Heliyon 9 (2023) e16397

Contents lists available at ScienceDirect

Heliyon

journal homepage: www.cell.com/heliyon

Research article

# $Fe_3O_4$@BNPs@ZnO–ZnS as a novel, reusable and efficient photocatalyst for dye removal from synthetic and textile wastewaters

Minoo Khodamorady [a], Kiumars Bahrami [a,b,*]

[a] Department of Organic Chemistry, Faculty of Chemistry, Razi University, Kermanshah 67144-14971, Iran
[b] Nanoscience and Nanotechnology Research Center (NNRC), Razi University, Kermanshah 67144-14971, Iran

ARTICLE INFO

*Keywords:*
$Fe_3O_4$@BNPs
Dye removal
Mercury lamp (UV and Visible light)
Photocatalyst
ZnO–ZnS hybrid

ABSTRACT

In this study, new magnetic nanocomposites with different molar ratios of zinc oxide-zinc sulfide were synthesized together with photocatalysts MNPs@BNPs@ZnO and MNPs@ BNPs@ ZnS. The photocatalytic behavior of these hybrid nanocomposites under visible light and ultraviolet light was investigated to remove methylene blue (MB), methyl orange (MO) dyes, real textile and carton effluents. After studies, the best active photocatalyst in both visible light and ultraviolet light is MNPs@BNPs@ZnO–ZnS (ZnO/ZnS: 0.75:0.25), which displayed the best performance in the ultraviolet region. According to the TEM, the average particle size for MNPs@BNPs@ZnO–ZnS (ZnO/ZnS: 0.75:0.25) is between 10 and 30 nm. Zeta potential (DLS) showed that the charge on the photocatalyst surface is negative at most pHs. PL analysis confirmed that the amount of hole-electron recombination in the optimal photocatalyst is less than MNPs@BNPs@ZnO and MNPs@BNPs@ZnS. Also, based on kinetic studies, the rate constant for removing azo dyes such as MO and MB was 0.0186 and 0.0171 $min^{-1}$, respectively. It is worth noting that in addition to the novelty of the synthesized photocatalysts, the UV and visible lamps used in this research are inexpensive, durable, and highly efficient.

## 1. Introduction

Water pollution is one of the most important environmental problems that the world is facing today, despite significant advances in science and technology.

Lack of fresh water resources on the one hand and uncontrolled discharge of organic pollutants such as paints into the water on the other hand has made wastewater purification one of the main challenges of the last decade [1–3].

The paper industry, dyeing, textile, cosmetics and food industries are among the industries that release large amounts of different colors into the environment. Disposal of these effluents poses significant risks to public health and the health of ecosystems [4,5].

One of the most important organic pollutants is dyes, which are often synthetic and have complex structures. Dyes, which are mostly toxic and carcinogenic, not only affect photosynthesis in aquatic ecosystems and inhibit aquatic growth, but also disrupt the reproductive process and cause defects in the central nervous system [6,7].

One of the processes that plays a key role in wastewater treatment today is the advanced oxidation process, which produces many

* Corresponding author. Department of Organic Chemistry, Faculty of Chemistry, Razi University, Kermanshah 67144-14971, Iran.
*E-mail address:* k.bahrami@razi.ac.ir (K. Bahrami).

https://doi.org/10.1016/j.heliyon.2023.e16397
Received 10 September 2022; Received in revised form 7 April 2023; Accepted 15 May 2023
Available online 20 May 2023

reactive radicals. These active radicals can easily destroy and remove organic pollutants and dyes without the need for special technology.

So far, various methods have been reported in the scientific literature for water treatment, among which, nanostructured photocatalysts and porous materials have received much attention [7].

Recently, metal oxides such as $TiO_2$, $SnO_2$, ZnO, CuO, $Bi_2WO_6$ and ZnS in nano dimensions have attracted much attention from researchers due to their usefulness in wastewater treatment as photocatalysts [8–13].

Hetero-metallic oxides are interesting candidates for use in photocatalytic processes due to their acid-base and redox properties. These hetero-metal oxides have large surface area, active sites, and high surface energy, which causes the production of a large number of photons in the photocatalytic reaction. So far, various hetero-metallic oxides have been reported to deal with the degradation of organic dyes in water treatment [14].

Meanwhile, ZnO is one of the most widely used metal oxides, which has advantages such as high activity, high photosensitivity, large exciton binding energy, ease of crystallization, low production cost, non-toxicity and versatility in synthesis [15–19]. ZnO exhibits better photocatalytic performance than $TiO_2$ due to its higher quantum efficiency. However, pure ZnO has disadvantages such as high band gap, high rate of electron–hole recombination, low ability to absorb sunlight and lack of activity in the visible light region. Therefore, to overcome these disadvantages, noble metals, semiconductors with a low band gap, and elemental doping can be used to modify ZnO [19,20]. Also, the green biosynthesis of binary metal oxide nanocomposites with distinct morphologies and structures is being developed as photocatalysts. So far, researchers have used many biological sources for the biosynthesis of metal oxide, such as; plant extracts, actinomycetes, fungi, yeasts, bacteria, macroalgae and viruses have been used [21–28].

The synthesis of nanocomposites with inconsistent structure by combining zinc oxide with other metal oxide or sulfides such as ZnS, CdS, CuO, AgO, and various metals and non-metals such as Ag, Sm, Co, O, Nd and N,. reduce the band gap and increase synergistic electronic and structural properties [29–37]. Important applications of ZnS include being used as an optical conductor, optical coating, modulator, optical coating sensor, dielectric filter, and light emitter [38,39].

Spinels are a group of metal oxides with $AB_2O_4$ structures, in which A and B are cations with different crystal structures, where (A = Mn, Fe, Co, Ni, Cu and Zn). Metal oxides with spinel structures have superparamagnetic properties and have many applications such as use as catalysts, use in electronic devices such as use as sensors and biosensors and energy storage, biomedical applications such as drug delivery, drug release and diagnosis, and use in water treatment [40].

In photocatalytic processes, centrifugation and filtration are used to separate the photocatalyst from the refined systems. These methods are not only time-consuming and expensive, but also limit the application of photocatalysts on a large scale [41]. A suitable solution to solve this problem is to combine photocatalysts with magnetic materials so that photocatalysts can be easily isolated and recovered on a large industrial scale [42].

Iron nanoparticles ($Fe_3O_4$) with spinel structure have been highly regarded by researchers in various fields due to their unique properties such as low toxicity, small size, and superparamagnetic behavior. Besides, usage of iron nanoparticles not only facilitates the separation of the catalyst from the media but also plays a significant role in catalyst recovery [43].

Boehmite (aluminium oxyhydroxide) is one of the solid, stable, reasonably priced and recyclable substrates that due to the large number of hydroxide groups on its surface, its surface can be easily modified with different groups and linkers. It is also worth noting that in photocatalytic processes and water treatment, the hydrophilicity of the photocatalyst support can be effective. Boehmite has many hydroxyl groups on its surface and is a hydrophilic support [43,44]. According to the explanation given above, in this study we synthesized magnetic boehmite nanoparticles with core-shell structure. The hybridization of boehmite nanoparticles (BNPs) with iron nanoparticles ($Fe_3O_4$ with spinel structure) not only increases the chemical and mechanical stability, but also increases the hydrophilic property of the substrate, which is an important feature in increasing the efficiency of the photocatalyst.

Due to the great importance of core-shell heterostructures, various techniques have been used for the synthesis [23,29,33–37] of heterogeneous ZnO–ZnS structure. For example, Liu et al. [45], synthesize of γ-$Fe_2O_3$/ZnO double-shelled hollow and used it for dye removal of MB, RhB, and MO. Xie et al. [46]. Prepared α-$Fe_2O_3$/ZnOphotocatalysts with various mole ratios of α-Fe2O3 to ZnO by a simplerefluxing method and used them for degradation of pentachlorophenol. Sanad et al. used ZnS–ZnO nanocomposite to remove methylene blue and Eosin dyes [47]. In another report, Hitkari research group studied the photocatalytic activity of ZnO/ZnS and ZnO/ZnS/α-$Fe_2O_3$ nanocomposites in MO degradation [48]. Recently, Xu's research group synthesized and investigated the photocatalytic effect of $Fe_3O_4$@$SiO_2$@ZnO/ZnS core/shell heterostructure in the photocatalytic degradation of organic pollutants such as TC, MB and RhB [49].

According to the above, in this study, a novel modified magnetic nanocomposite (modified magnetic bohemite with core-shell structure containing zinc oxide-zinc sulfide) was designed and synthesized. The introduced photocatalyst has advantages such as cheapness, stability, easy synthesis method and environmentally friendly. The novel introduced nanocatalyst in this research ($Fe_3O_4$@BNPs-ZnO-ZnS) was evaluated for dye removal from synthetic and real wastewaters (colored wastewaters of Kermanshah carton factory and Kashan textile factory) in both visible and ultraviolet regions.

It is worth mentioning that after the studies, it was found that the introduced photocatalyst is active in both UV and visible region, but is very efficient in the UV region. Also, as an advantage, the light source used in this research is a high-pressure mercury lamp, which is very cheap, durable and with excellent efficiency in removing organic pollutants compared to other lamps on the market.

## 2. Experimental

### 2.1. Materials and methods

All materials and reagents were purchased from Merck company with high purity and did not need to be purified. Materials used in this study are hydrated aluminum nitrate.

($Al(NO_3)_3{\cdot}9H_2O$) (98.5%), sodium hydroxide (NaOH) (97%), iron chloride ($FeCl_3$) (99%), iron sulfate ($FeSO_4$) (98%), zinc acetate ($Zn(OAc)_2$) (99.5%), sodium sulfide ($Na_2S$), ethanol (99%), ascorbic acid (AA) (99%), Isopropyl alcohol (IPA) (99.8%), citric acid (CA) (99.5%), sodium nitrate ($NaNO_3$) (99.5%), methylene blue dye ($C_{16}H_{18}ClN_3S$) and methyl orange dye ($C_{14}H_{14}N_3NaO_3S$). The lamps used in this study are high-pressure mercury vapor lamps as a visible light source and high-pressure mercury vapor lamps without a bulb (the bubble is carefully broken) as an ultraviolet light source (equivalent to 350–380 nm). Shimadzu IR-470 spectrometer was used to record the FT-IR spectra. FESEM pictures of MNPs and photocatalyst were performed by a TESCAN-MIRA3. Quantitative analysis was performed by energy dispersive spectrometry (EDS). TGA diagram was recorded on the STA504 in the temperature range of 25–800 °C at a heating rate of 10 °C $min^{-1}$. XRD patterns of samples were recorded on a JEOL-JDX–8030 (30 kV, 20 mA). Zeta potential was recorded on SZ-100z Dynamic Light Scattering & Zeta potential analyze (Horiba Jobin). The DRS spectrum of $Fe_3O_4$@BNPs@ZnO–ZnS was recorded by Avaspec-2048-TEC. VSM + FORC vibrating sample magnetometer was used to measure the magnetic property of the photocatalyst. Also, photoluminescence spectra were obtained by PerkinElmer LS55. Degradation experiments were monitored by UV–visible absorption spectroscopy (UV–1650PC SHIMADZU, Columbia, MD, USA). Photochemical experiments were carried out using a high-pressure mercury lamp (125 W) with $\lambda > 400$ nm. HR-TEM FEI TECNAI F20 apparatus was used to record HR-TEM images. TOC was performed with a Shimadzu TOC-5000-A systemequipped with a non-dispersive infrared detector. The ICP-OES analysis was recorded on PerkinElmer DV 5300. XPS spectra were obtained with UHV analysis system.

### 2.2. Synthesis of $Fe_3O_4$@BNPs@ZnO–ZnS

To synthesize modified magnetic boehmite with zinc oxide-zinc sulfide, a mixture of ferric chloride, ferrous sulfate and 25 mL of sodium hydroxide solution (1.25 g of NaOH in 25 mL of $H_2O$: 5% w/v) is first mixed and placed under nitrogen gas at 90 °C for 2 h. After synthesis, the $Fe_3O_4$ nanoparticles (MNPs) were separated by an external magnet, washed with water and ethanol. In the next step, a solution of aluminum nitrate was added to MNPs and then the sodium hydroxide solution (10%) was added dropwise and the mixture was placed in an ultrasonic bath for 1 h [43]. Then, a solution of zinc acetate was added to the magnetic boehmite and refluxed at room temperature for 1 h after sonication. A solution of NaOH and sodium sulfide (dissolved in 20 mL of water and ethanol) was then added to the mixture and the mixture was refluxed for 2 h at 60 °C. The mixture was cooled then $Fe_3O_4$@BNPs@ZnO–ZnS was separated by a strong magnet, rinsed several times with water and dried at 60 °C [49,50].

### 2.3. Procedure for the synthesis of $Fe_3O_4$@BNPs@ZnO

A solution of zinc acetate was added to the $Fe_3O_4$@BNPs under sonication and the mixture was refluxed at room temperature for 1 h. After that, solutions of sodium sulfide and sodium hydroxide were added to the mixture and the mixture was refluxed at 60 °C. The synthesized $Fe_3O_4$@BNPs@ZnO nanocomposite, after cooling, was separated by a strong external magnet, washed with water and dried in an oven at 60 °C [19].

### 2.4. Synthesis of $Fe_3O_4$@BNPs@ZnS

Zinc acetate solution was added to $Fe_3O_4$@BNPs by sonication and the mixture was refluxed at room temperature for 1 h under intense stirrer. A solution of $Na_2S$ was then added and the mixture was refluxed again at 60 °C for 2 h. The prepared $Fe_3O_4$@BNPs@ZnS nanoparticles were cooled, separated by an external magnet and dried after rinsing with water at 60 °C [47,48].

### 2.5. Dye removal experiments of synthetic methylene blue and methyl orange solutions

In order to evaluate the performance of photocatalysts, aqueous solutions of methylene blue and methyl orange with concentrations of 10, 15 and 20 ppm were prepared. After the appropriate time, the photocatalyst was quickly (less than 20 s) separated from the environment by a strong external magnet. Then, about 2 mL of the solution was withdrawn by a pipette and the change in absorption of the dye solution was checked by UV–Vis spectrophotometer (UV–1650PC SHIMADZU, Columbia, MD, USA).

The effects of various parameters such as photocatalyst amount, dye concentration and ambient pH were investigated. After conducting studies, the optimal photocatalyst was selected and the performance of the photocatalyst in photocatalytic dye removal of the effluent of Kermanshah carton company (relatively thick olive effluent which is a mixture of several colors black, yellow, red and white) was investigated. Also, real effluents such as sausage, dark benton and dark olive related to Kashan textile factory with concentrations of 15–20 ppm were reviewed.

Also, radical scavengers such as ascorbic acid (AA), Isopropyl alcohol (IPA), sodium nitrate, and citric acid (CA) were added to the solutions as scavengers for, $O_2^-$, OH, $e^-$ and $h^+$, respectively.

## 3. Results and discussion

In this research work, in addition to three photocatalysts with different molar ratios of zinc oxide and zinc sulfide for $Fe_3O_4$@BNPs @ ZnO–ZnS (ZnO/ZnS = 0.25/0.75, ZnO/ZnS = 0.5/0.5, ZnO/ZnS = 0.75/0.25), $Fe_3O_4$@BNPs@ZnO and $Fe_3O_4$@BNPs@ZnS were also synthesized.

Based on the predictions and laboratory studies, it was found that the higher the percentage of zinc oxide on the surface, the more active the photocatalyst in the ultraviolet region. Based on this, $Fe_3O_4$@BNPs@ ZnO–ZnS photocatalyst with ZnO/ZnS molar ratio = 0.75/0.25 was selected and identified as a more active photocatalyst with more efficiency in the ultraviolet region.

### 3.1. $Fe_3O_4$@BNPs@ZnO–ZnS characterization methods

Different analyzes such as FTIR, TGA, XRD, SEM, FESEM, TEM, HR-TEM, EDX, Mapping, XPS, ICP-OES, PL, VSM, BET, DRS, Zeta potential were performed to confirm the structure and evaluate the properties of the best photocatalyst. All steps of photocatalyst synthesis are shown in detail in Scheme 1.

Fig. 1 shows the infrared spectra of $Fe_3O_4$, $Fe_3O_4$@BNPs@ZnO, $Fe_3O_4$ @BNPs@ZnS and $Fe_3O_4$ @BNPs@ZnO–ZnS photocatalyst with molar ratio ZnO/ZnS = 0.75/0.25. In the IR spectrum of $Fe_3O_4$ @BNPs@ZnS (blue curve), the appeared stretching vibrations of 610.1 and 1132.5 $cm^{-1}$ are due to ZnS. Also, the OH bending frequency has appeared in 1619.2 $cm^{-1}$. The vibration shown at 3418.2 $cm^{-1}$ is related to the OH groups of $Fe_3O_4$ NPs [51]. In the IR spectrum of $Fe_3O_4$ @BNPs@ZnO (pink curve), the frequencies appearing at 478.1 and 587.2 $cm^{-1}$ correspond to ZnO. Also, OH bending frequency is appeared at 1618.5 $cm^{-1}$ and stretching vibrations at 3415.5 and 3475.1 $cm^{-1}$ are related to the hydroxyl groups on the surface of $Fe_3O_4$ NPs and water molecules [51].

As can be seen from the IR spectrum of $Fe_3O_4$ NPs, the vibrational frequency appearing in 480.1 $cm^{-1}$ is related to the octahedral Fe–O tensile vibration and the absorption band at 621.9 are related to the Fe–O tetrahedral tensile vibration. The tensile vibration appearing in 1133.6 $cm^{-1}$ is associated to the hydroxyl group of the water molecule. The peak appearing in 1618.5 $cm^{-1}$ also belongs to the bending vibration of the hydroxyl group. The vibrations appearing in 3416.1 and 3475.6 $cm^{-1}$ are related to the hydroxyl groups on the surface of iron nanoparticles and water molecules [51]. In the FT-IR spectrum of $Fe_3O_4$@BNPs@ZnO–ZnS, the vibrations at 477.1 and 617.9 $cm^{-1}$ are related to Zn–O and Fe–O, respectively [52]. The peak appearing on 1619.9 $cm^{-1}$ is related to the bending vibration of the hydroxyl group. The absorptions appearing in 3416.2 and 3474.1 $cm^{-1}$ are attributed to the hydroxyl groups on the surface of iron nanoparticles and water molecules (Fig. 1, green curve).

The XRD spectra of magnetic boehmite nanoparticles and $Fe_3O_4$@BNPs@ZnO–ZnS NPs are shown in Fig. 2. In the XRD pattern of MNPs, peaks appeared in 30.38, 35.79, 43.49, 53.92, 57.45 and 63.00 (01-075-0449 JCPDS No.), which have Miller coefficients of (440), (511), (422), (400), (311), (220), respectively. According to the XRD spectrum, the structure of the MNPs is cubic. The peaks appearing at 37.51 and 72.72 affirm the presence of boehmite nanoparticles in the structure. In the XRD curve for the MNPs@BNPs@ZnO–ZnS photocatalyst, the peaks at 28.92 (111),47.62 (220) and 56.64 (311) are related to cubic phase of ZnS [53] (JCPDS No. 01- 080-0020). The ZnS crystallite size was found to be 26.6 nm using the Debye Scherrer [54] (equation (1)) for the (311) plane.

$$D = K\lambda/\beta\, Cos\, \Theta \tag{1}$$

Here, $D$ is the crystallite size, $K$ is the shape factor, calculated for spherical particles is 0.9, $K = 1.54$ A° for Cu and $\beta$ is full width at half maxima of the highest peak in radian.

Also, the peaks seen in 31.73 (100), 34.31 (002), 36.20 (101), 48.33 (102), 62.96 (103) corroborate the presence of hexagonal ZnO in the photocatalyst structure [55] (JCPDS No. 01-080-0075) (Fig. 2). The calculated crystallite size for ZnO using (103) diffraction peak was 22.6 nm (Fig. S1, Pdf files of XRD in supplementary data).

In order to understand the structure and size of photocatalyst particles, FESEM and particle size distribution histograms were used. According to FESEM images, the structure of MNPs@BNPs is almost spherical and the distribution of particles is uniform and the

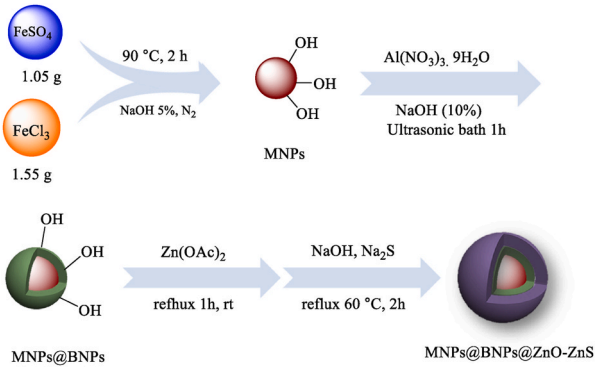


**Scheme 1.** Schematic synthesis of MNPs@BNPs@ZnO–ZnS.

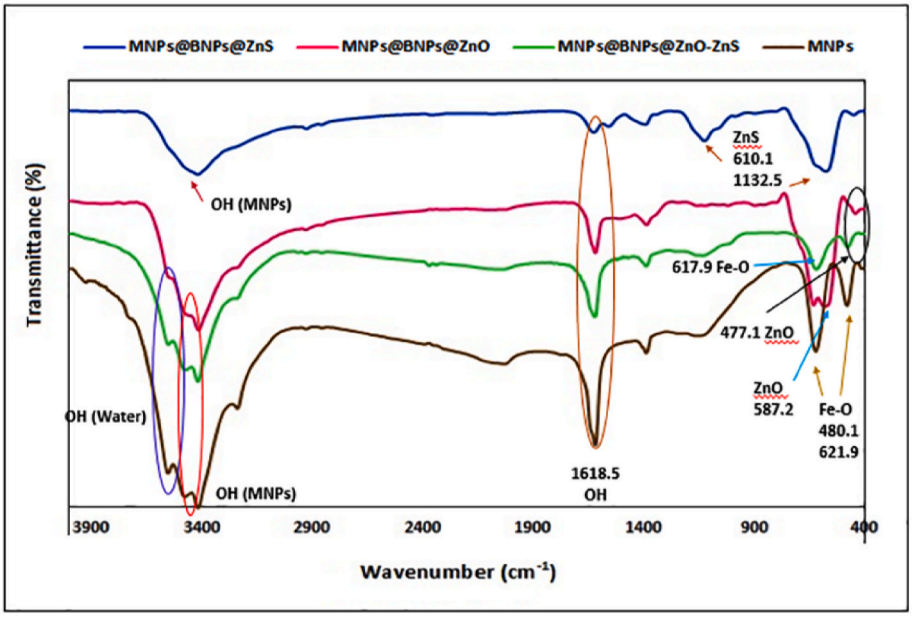


**Fig. 1.** FT-IR spectra of MNPs (brown), MNPs@BNPs@ZnO–ZnS (green), MNPs@BNPs@ZnO (pink), and MNPs@BNPs@ZnS (blue). (For interpretation of the references to color in this figure legend, the reader is referred to the Web version of this article.)

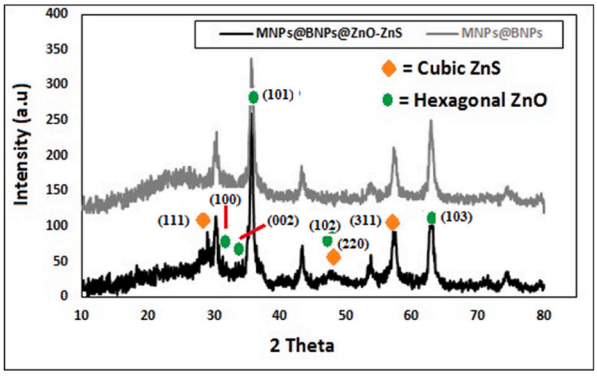


**Fig. 2.** XRD patterns of MNPs@BNPs and MNPs@BNPs@ZnO–ZnS.

average particle size is 40–50 nm (Fig. 3a). As can be seen from Fig. 3b, after fixing the ZnO–ZnS hybrid on the surface of magnetic boehmite (MNPs@BNPs), the spherical structure is preserved and the particle distribution is almost uniform everywhere. Also, SEM was taken from the MNPs@BNPs@ZnO and MNPs@BNPs@ZnS samples (Fig. 3c and d) for a better comparison of the synthesized photocatalysts. Based on Fig. 3c and d, the nanoparticles have an almost uniform distribution and their shape is close to spherical. The particle distribution histogram obtained from FESEM was used to calculate the exact particle size and show the particle size distribution. Based on the photocatalytic histogram of $Fe_3O_4$@BNPs @ ZnO–ZnS with a molar ratio of ZnO/ZnS = 0.75/0.25 (Fig. 3e), particles with a size of 30–50 nm have the highest frequency. TEM analysis was used to confirm the photocatalyst core-shell structure and obtain the exact particle size. The TEM image of the nanocomposite (Fig. 3f) well confirms that the core-shell structure has been synthesized and the particles are regularly and uniformly dispersed. According to TEM, the particle size was between 10 and 25 nm, which is in good agreement with the particle size obtained from the Debye Scherrer equation has it. In Fig. 3g, the HR-TEM image is shown, in which the crystalline planes of zinc oxide and zinc sulfide can be distinguished. In the SAED pattern of $Fe_3O_4$@BNPs@ZnO–ZnS (Fig. 3h), all diffraction rings correspond to (100), (002), (101), (102), (103) planes of ZnO and (111), (220), (311) planes of ZnS nanoparticles are visible. Also, the SAED analysis shows the polycrystalline structure of the nanocomposite, which is in consistent with the XRD results.

Another technique used to confirm the successful synthesis of photocatalyst is EDX analysis, in which all the major elements in the photocatalyst structure such as Fe, Al, O, S, Zn appear (Fig. 4a). EDS-Mapping technique was used to confirm the synthesis of photocatalyst and to find out the presence of all the main elements in the texture of the sample. As can be seen from Fig. 4b–g, all the main elements such as Fe, Al, Zn, O, and S are present and are uniformly dispersed in the photocatalyst structure.

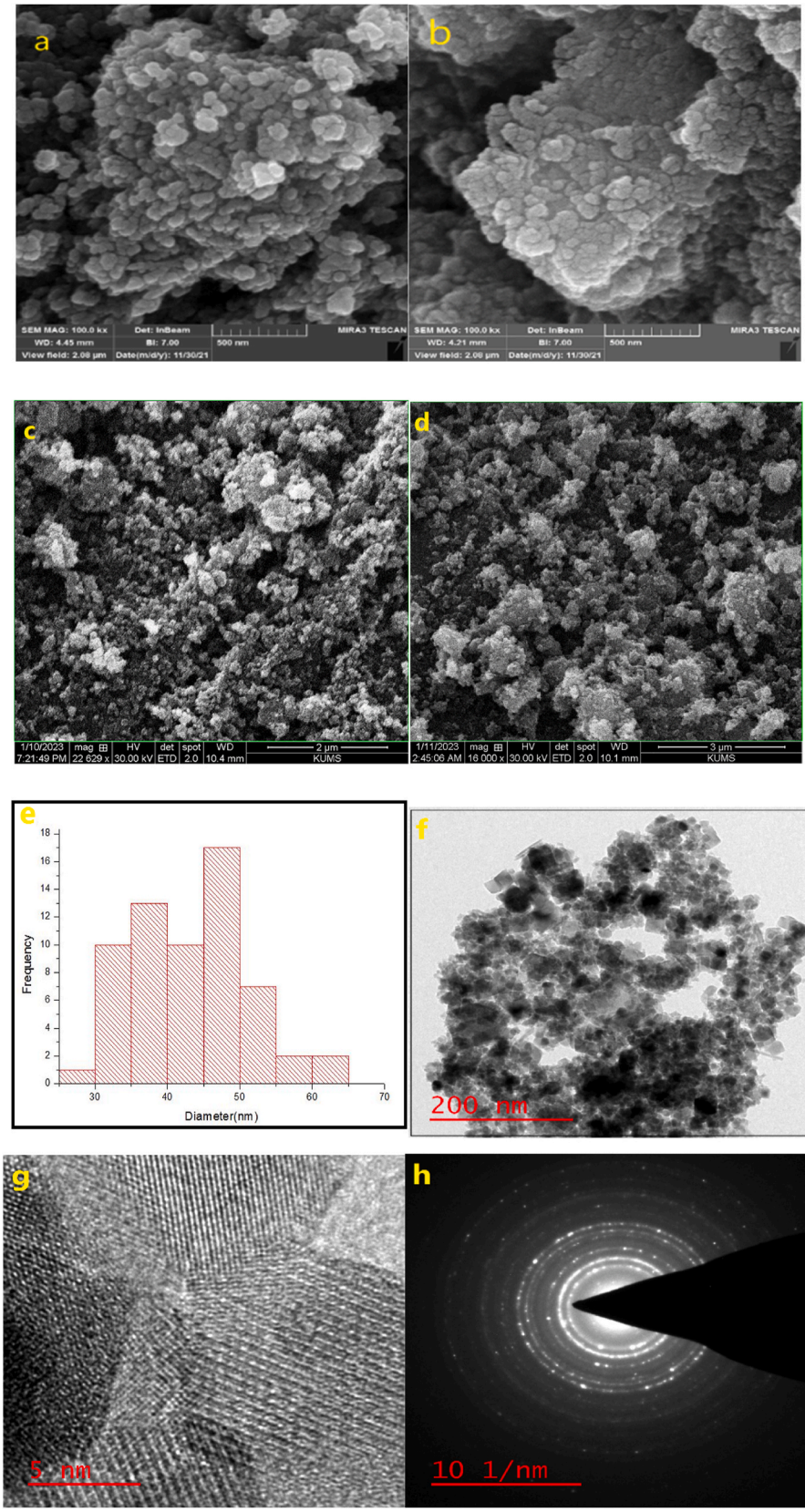


*(caption on next page)*

**Fig. 3.** FESEM images of (a) MNPs@BNPs, (b) MNPS@BNPs@ZnO–ZnS and (c) histogram size distribution of MNPs@BNPs@ZnO–ZnS, (d) SEM image of MNPs@BNPs@ZnO, (e) SEM image of MNPs@BNPs@ZnS, (f) TEM of MNPS@BNPs@ZnO–ZnS, (g) HR-TEM of photocatalyst, and (h) SAED pattern of MNPS@BNPs@ZnO–ZnS.

With the help of photoluminescence spectroscopy, the amount of electron-hole recombination can be obtained. In this way, the shorter the height of the emission spectrum, the lower the electron-hole recombination rate, and the higher the photocatalyst efficiency. As can be seen from Fig. 5a, MNPs@BNPs@ZnO–ZnS photocatalyst have lower electron-hole recombination rates than MNPs@BNP@ZnO and MNPs@BNPs@ZnS photocatalysts. The lower the recombination rate, the higher the photocatalyst efficiency. DRS spectrum and band gap of the prepared MNPs@BNPs@ ZnO–ZnS are shown in Fig. 5b and c, respectively. Band gap was calculated using Tauc plots. The intercept of the tangent to the plot of $(\alpha h\upsilon)^{0.5}$ versus (Eg) expresses the energy of the band gap with a good approximation. It is worth noting that the band gap for synthesized nanocomposites is much shorter compared to the band gap for zinc oxide and zinc sulfide, which are 3.3 [56] and 3.6 [57], respectively.

Based on BET test specific surface area (64.86 $m^2/g$), particle volume (14.90 $cm^3/g$), total pore volume (0.165 $cm^3/g$) and mean pore diameter (10.173 nm) for optimal photocatalyst MNPs@BNPs@ZnO–ZnS with ZnO/ZnS molar ratio: 0.75/0.25 were obtained. The values of BET surface area, mean pore diameter and total pore volume for MNPs@BNPs@ZnS are 89.77 $m^2/g$, 12.89 nm, and 0.161 $cm^3/g$, respectively, and these values for MNPs@BNPs@ZnO are 58.82 $m^2/g$, 15.63 nm, and 0.267 $cm^3/g$, respectively. By comparing the values obtained from BET analysis, the specific surface area of nanocomposite is higher than MNPs@BNPs@ZnO but lower than MNPs@BNPs@ZnS, and the average pore diameter of nanocomposite is lower than the values obtained for ZnO and ZnS samples.

Also, based on Langmuir test, particle volume (16.796 $cm^3/g$) and specific surface area of 73.105 $m^2/g$ were obtained. The higher the specific surface area of the MNPs@BNPs ZnO–ZnS nanocomposite, the higher the photocatalyst efficiency.

The nitrogen absorption and desorption (Fig. 6) shows that the synthesized photocatalyst follows the type 4 (IV) isotherm, which has a mesoporous structure based on the AUPAC classification.

The magnetic strength of MNPs@BNPs and MNPs@BNPs@ ZnO–ZnS with ZnO/ZnS ratio 0.75/0.25 are shown in Fig. 7. The magnetic boehmite strength is 63.15 emu/g and the magnetic strength of the photocatalyst is 27.25 emu/g, which confirms the very high magnetic strength of this photocatalyst as a result of its successful synthesis. The higher the magnetic strength, the easier it is to separate the catalyst from the reaction medium.

The zeta potential technique was used to know the charge on the photocatalyst surface. At several different pHs (3, 5, and 8), zeta potential (DLS) was taken, and Gaussian diagrams of zeta potential for the MNPs@BNPs@ZnO–ZnS are shown in supporting information file (Fig. 2S). Numerical values of zeta potential at pHs 3, 5 and 8 are also listed in Table 1. Since the charge on the photocatalyst surface is negative at all pHs, the photocatalyst shows a better performance in removing cationic dyes than anionic dyes.

The thermal stability of the photocatalyst was evaluated by TGA technique under argon atmosphere. As Fig. 8 shows, weight loss occurs in three stages. In the range of 0–125 °C, the adsorbed water and organic solvents evaporate (about 2.5%). Subsequent failures occur in the range of 100–350 °C due to chemical transformations and physical changes such as the removal of ZnO from the photocatalyst surface, the transformation of ZnS structure to wurtzite structure, and the separation of ZnS from the nanocomposite surface. (1.5%) [58,59]. Also, from 350 to 450 °C, about 2.14% of the weight is lost, which is linked to the decomposition of the core shell structure and the change of the boehmite crystal phase [43,60].

X-ray photoelectron spectroscopy (XPS) was used to find out the chemical states and surface composition of $Fe_3O_4$@BNPs@ZnO–ZnS nanoparticles. Fig. 9b shows that Zn $2p_{3/2}$ and Zn $2p_{1/2}$ peaks are observed at 1021.8 and 1045.15 eV, respectively [50,61]. As Fig. 9c shown, the two main peaks located at 711.60 and 725.25 eV are related to Fe $2p_{3/2}$ and Fe $2p_{1/2}$ spin orbitals, respectively, while their satellite peaks appear at 717.19 and 732.45 eV, respectively. It should be mentioned that these appeared peaks are in perfect agreement with the standard peak of iron nanoparticles [62]. The presence of the peak at 530.5 eV confirms the presence of oxygen in the ZnO compound and crystalline oxygen in the structure of $Fe_3O_4$ [63] (Fig. 9d). The observed peak at 89.60 eV affirms the presence of Al 2p in the nanocomposite structure [64] (Fig. 9e). As can be seen from Fig. 9f, two peaks appeared at 160.70 and 161.60 eV, which correspond to S $2p_{1/2}$ and S $2p_{3/2}$ of $S^{-2}$ in the photocatalyst structure [50,65], respectively.

High-pressure mercury bulbs without bulbs (the bulb was carefully broken) were used as the ultraviolet light source, and high-pressure mercury bulbs were used as the visible light source (see supplementary data Fig. S3).

### 3.2. Kinetic studies

In order to find the best photocatalyst, studies were performed with aqueous solutions of methylene blue and methyl orange with a concentration of 10 ppm in the presence of the above-mentioned photocatalysts. Next, the photocatalytic effect of the magnetic boehmite (MNPs@BNPs) was investigated in the degradation of methylene blue and methyl orange dyes in the presence of a high-pressure mercury lamp as a UV light source (Table 2, entries 21–22). Based on the obtained results, in the presence of MNPs@BNPs, 14% dye removal for methylene blue and 3% for methyl orange was obtained. The important point here is that the MNPs@BNPs acted as a dye absorbent in the removal of methylene blue dye and did not show a photocatalytic effect. According to the evidence, MNPs@BNPs does not have a special role in the photocatalytic activity of the optimal MNPs@BNPs@ZnO–ZnS and the main photocatalytic activity is related to zinc oxide-sulfide stabilized on the surface of MNPs@BNPs. (Fig. S4, see the supporting file). The results are summarized in Table 2. Also, the efficiency of photocatalyst to remove MO and MB dyes was investigated under sunlight, and the related results are documented in Table 2, entries 23–24.

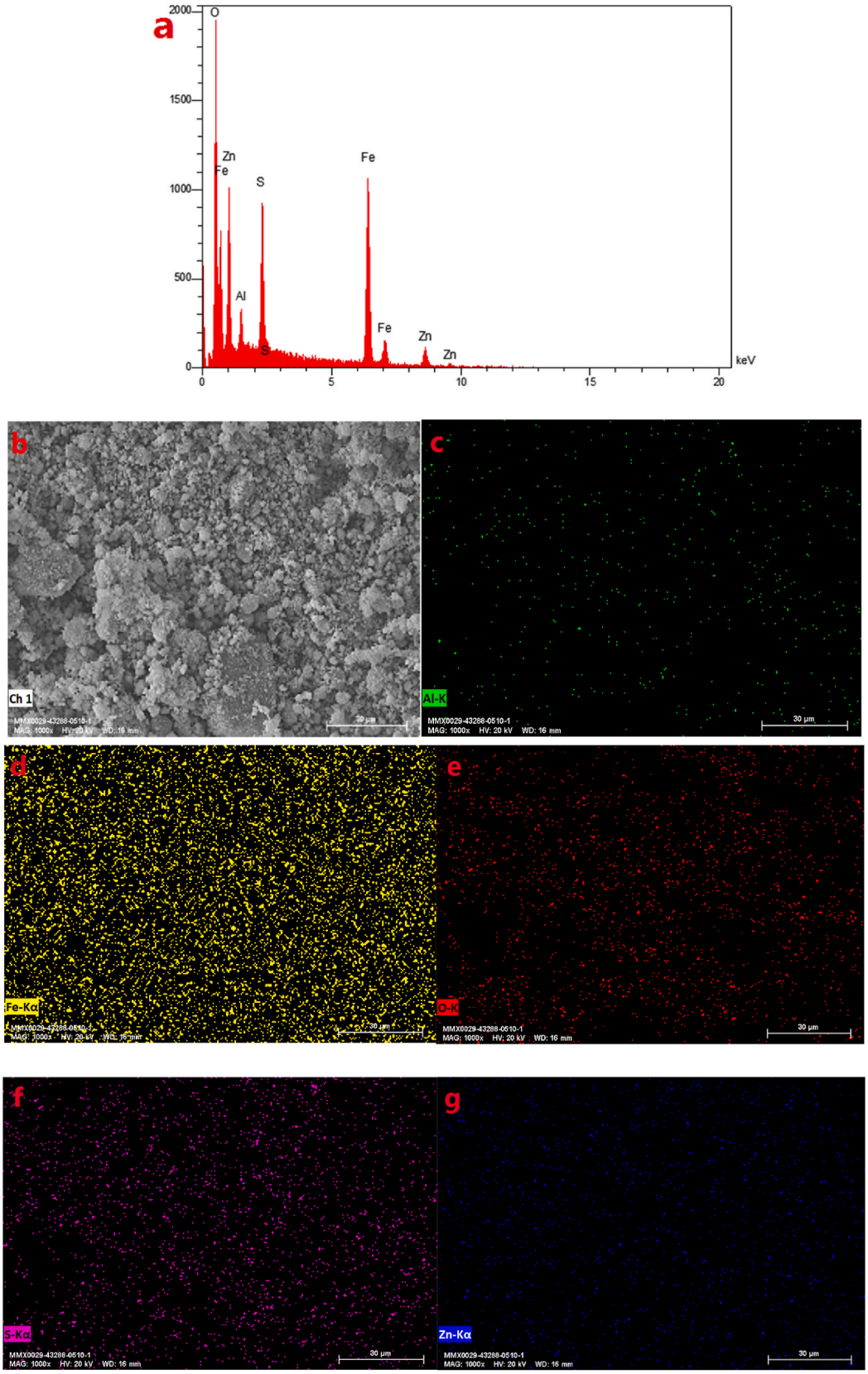


*(caption on next page)*

**Fig. 4.** (a) EDX pattern of MNPs@BNPs@ZnO–ZnS, and (b–g) EDS-Mapping of MNPs@BNPs@ZnO–ZnS.

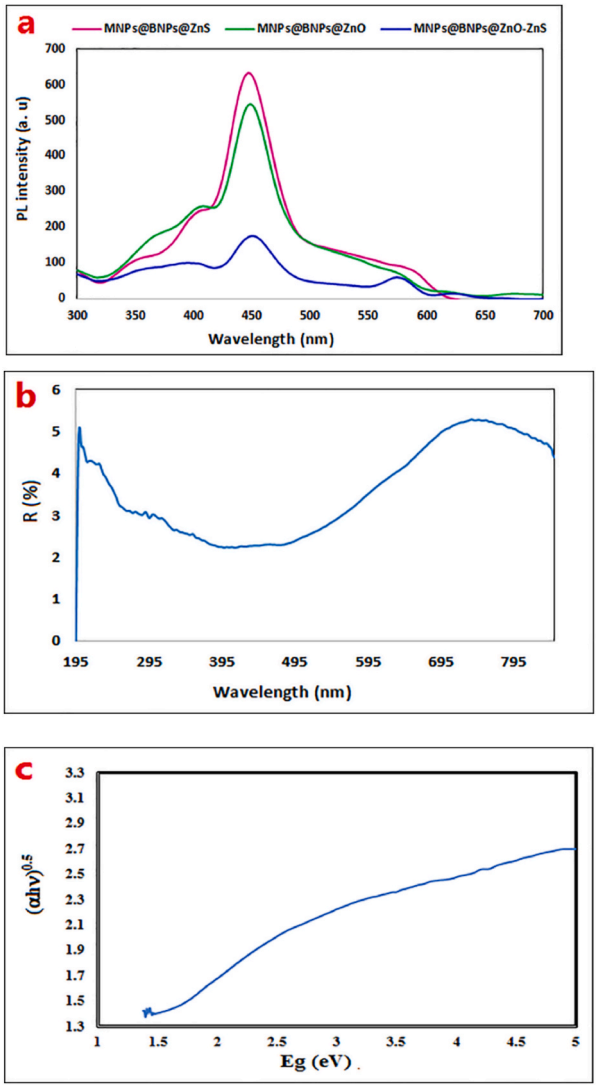


**Fig. 5.** (a) Photoluminescence spectra of MNPs@BNPs@ZnO–ZnS, MNPs@BNPs@ ZnO and MNPs@BNPs-ZnS, (b) DRS spectrum of nanocomposite and (c) Tauc plots of the MNPs@BNPs@ZnO–ZnS

As Table 2 displays, the best photocatalyst in the ultraviolet region is MNPs@BNPs@ZnO–ZnS with molar ratio (ZnO/ZnS = 0.75/0.25). As can be seen from Table 2, the MNPs@BNPs@ZnO–ZnS (0.75:0.25) is also active in the visible region, but the decolorization efficiency is lower compared to the UV region.

Then the amount of catalyst was optimized and for this purpose the values of 0.03, 0.05, 0.08 and 0.1 g of MNPs@BNPs@ZnO–ZnS were examined (Fig. S5, see the supporting file). The highest dye removal rate was obtained in the presence of 0.08 g of photocatalyst for both MB and MO.

A higher amount of photocatalyst has a little effect on the amount of dye removal (1–3%), which was chosen as the optimal amount of photocatalyst due to economic reasons and less waste of materials.

First, the decolorization reactions of methylene blue and methyl orange were investigated in the dark (in the absence of a high-pressure mercury lamp) in the presence of $Fe_3O_4$@BNPs-ZnO-ZnS. After 60 min, about 3% and 1% of MB and MO dyes were removed, respectively. Also, MB and MO dye removal reactions were exposed to high-pressure mercury lamp radiation for 1 h in the absence of photocatalyst. The amount of photolysis was 2% for MB and 1% for MO.

After optimizing the amount of photocatalyst and selecting the light source (high-pressure mercury lamp without bulb as ultraviolet light source), methylene blue (MB) and methyl orange (MO) dye removal tests were performed under ultraviolet light. After the specified irradiation time had elapsed, the catalyst was easily and quickly separated using an external magnet and 2 mL of the dye

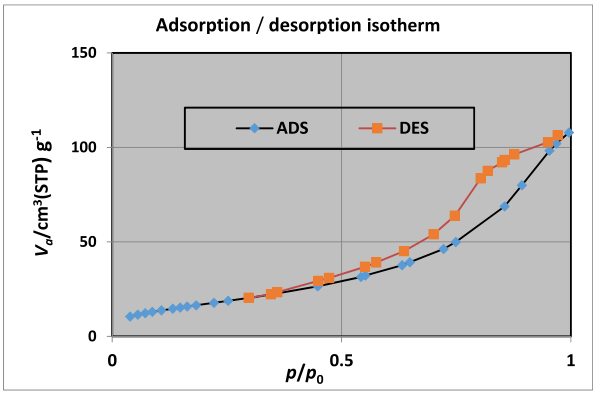


**Fig. 6.** Adsorption and desorption isotherm of the photocatalyst.

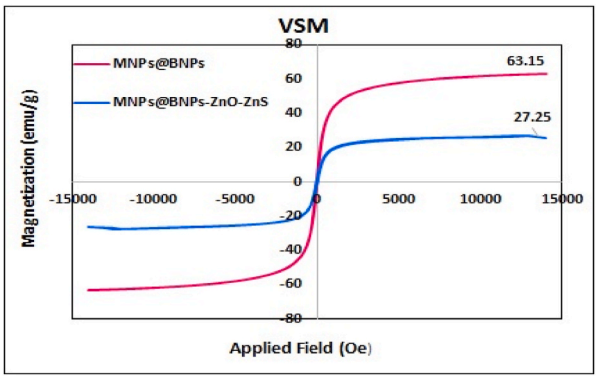


**Fig. 7.** VSM analysis of MNPs@BNPs@ZnO–ZnS in comparison with MNPs@BNPs.

**Table 1**
Zeta potential at pHs 3, 5 and 8.

| Entry | pH | Zeta potential |
|---|---|---|
| 1 | 3 | −2.5 mv |
| 2 | 5 | −11.5 mv |
| 3 | 8 | −17.2 mv |

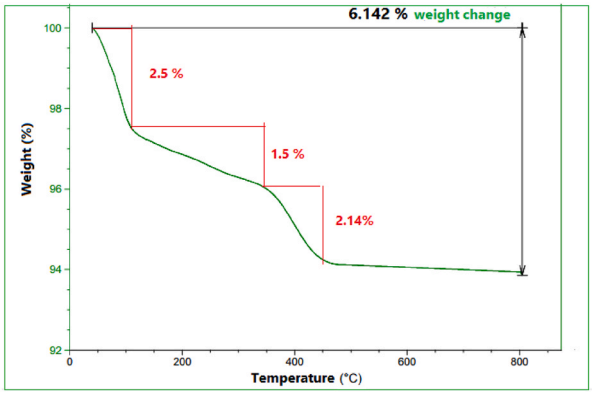


**Fig. 8.** TGA curve for the MNPs@BNPs@ZnO–ZnS.

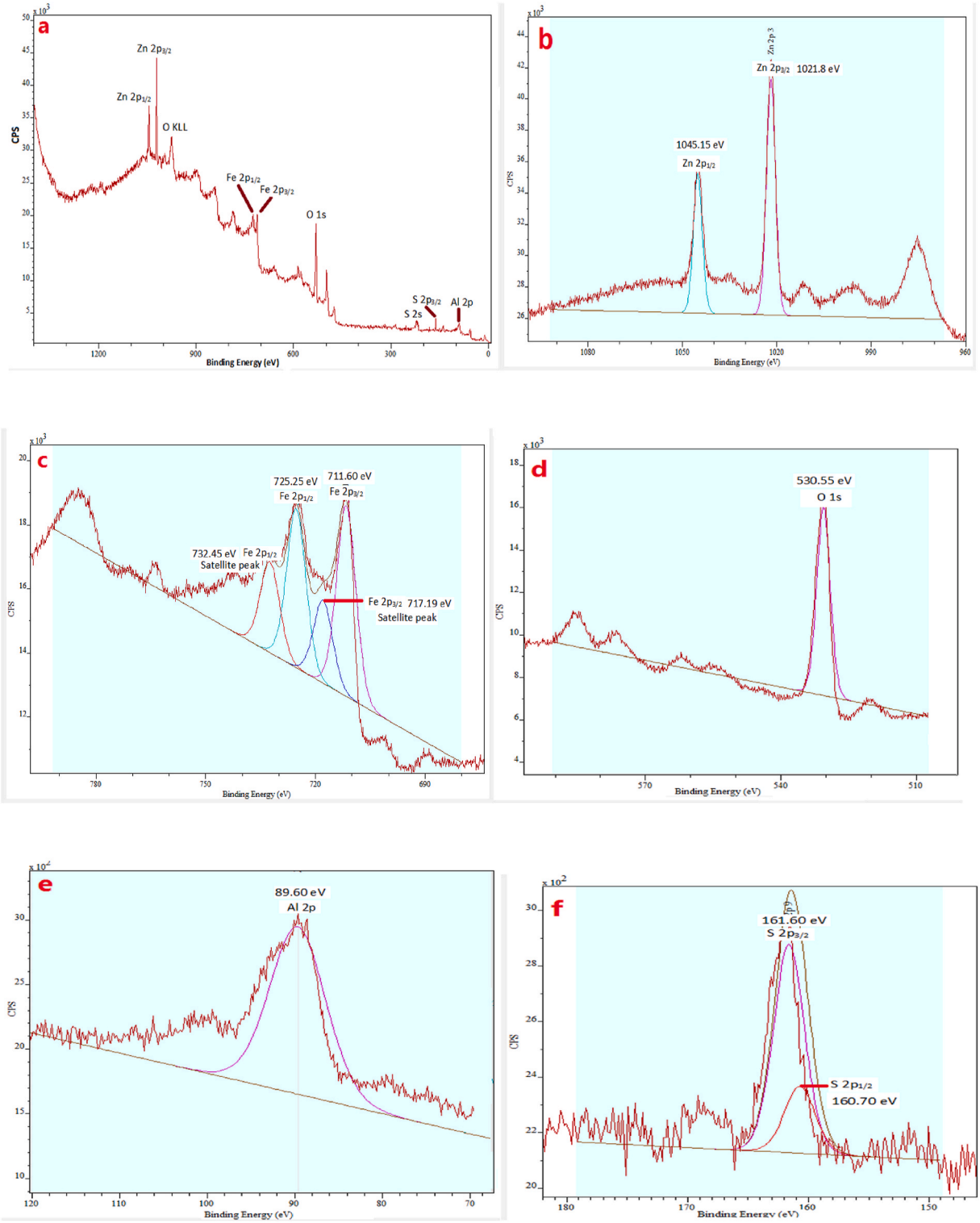


**Fig. 9.** XPS spectra of (a) photocatalyst, (b) binding energy for Zn 2p, (c) binding energy for Fe 2p, (d) binding energy for O 1s, (e) binding energy for Al 2p, and (f) binding energy for S 2p.

**Table 2**
Experiments to find the best photocatalyst in the ultraviolet and visible region.

| Entry | Catalyst[a] | Dye | Light | Dye removal (%) | Time (min) |
|---|---|---|---|---|---|
| 1 | MNPs@BNPs-ZnS | MB | Vis | 37 | 90 |
| 2 | MNPs@BNPs-ZnS | MB | UV | 25.4 | 90 |
| 3 | MNPs@BNPs-ZnS | MO | Vis | 33 | 90 |
| 4 | MNPs@BNPs-ZnS | MO | UV | 21 | 90 |
| 5 | MNPs@BNPs-ZnO | MB | Vis | 6 | 90 |
| 6 | MNPs@BNPs-ZnO | MB | UV | 10 | 90 |
| 7 | MNPs@BNPs-ZnO | MO | Vis | 4 | 90 |
| 8 | MNPs@BNPs-ZnO | MO | UV | 2.4 | 90 |
| 9 | MNPs@BNPs@ZnO–ZnS (0.25:0.75) | MB | Vis | 49.3 | 90 |
| 10 | MNPs@BNPs@ZnO–ZnS (0.25:0.75) | MB | UV | 47.6 | 90 |
| 11 | MNPs@BNPs@ZnO–ZnS (0.25:0.75) | MO | Vis | 58 | 90 |
| 12 | MNPs@BNPs@ZnO–ZnS (0.25:0.75) | MO | UV | 54.5 | 90 |
| 13 | MNPs@BNPs@ZnO–ZnS (0.5:0.5) | MB | Vis | 49.4 | 90 |
| 14 | MNPs@BNPs@ZnO–ZnS (0.5:0.5) | MB | UV | 47.2 | 90 |
| 15 | MNPs@BNPs@ZnO–ZnS (0.5:0.5) | MO | Vis | 48 | 90 |
| 16 | MNPs@BNPs@ZnO–ZnS (0.5:0.5) | MO | UV | 56.8 | 90 |
| 17 | MNPs@BNPs@ZnO–ZnS (0.75:0.25) | MB | Vis | 55 | 90 |
| 18 | MNPs@BNPs@ZnO–ZnS (0.75:0.25) | MB | UV | 80.5 | 90 |
| 19 | MNPs@BNPs@ZnO–ZnS (0.75:0.25) | MO | Vis | 48 | 90 |
| 20 | MNPs@BNPs@ZnO–ZnS (0.75:0.25) | MO | UV | 85 | 90 |
| 21 | MNPs@BNPs | MO | UV | 3 | 90 |
| 22 | MNPs@BNPs | MB | UV | 14 | 90 |
| 23 | MNPs@BNPs@ZnO–ZnS (0.75:0.25) | MO | Sun light | 5 | 120 |
| 24 | MNPs@BNPs@ZnO–ZnS (0.75:0.25) | MB | Sun light | 12 | 120 |

[a] gr of photocatalyst = 0.08 gr.

solution was sampled. To obtain the dye removal efficiency, the synthetic effluent was analyzed after catalyst separation by UV–Vis spectrophotometer. The following equation was used to obtain the color removal efficiency:

$$Removal\ (\%) = (A_0 - A_t / A_0) \times 100 \quad (2)$$

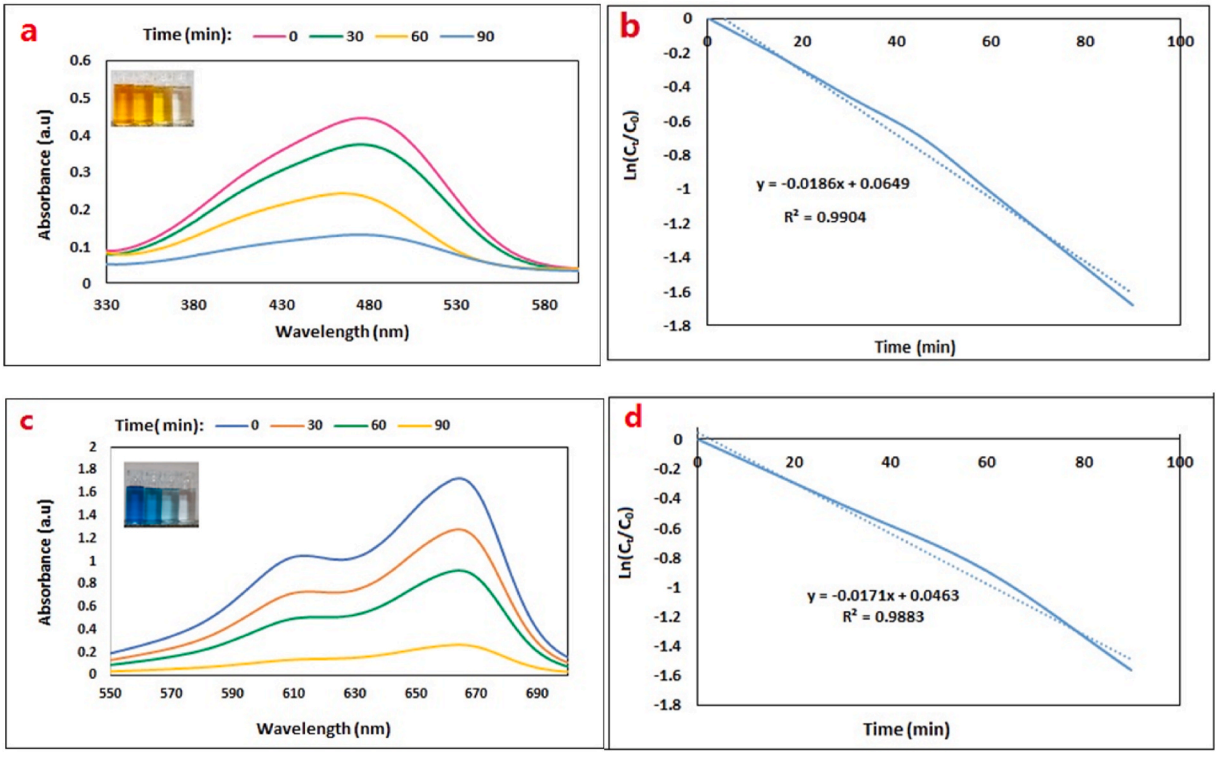


**Fig. 10.** Photocatalytic dye removal of (a) MO and (c) MB dyes and first order kinetic diagrams related to photocatalytic dye removal of (b) MO and (d) MB in the presence of MNPs@BNPs@ZnO–ZnS.

Where $A_0$ is the adsorption of the dye solution at time = 0 and $A_t$ is the adsorption of the final sample at time t.

Both MO and MB dyes showed high efficiency in the presence of MNPs@BNPs@ZnO–ZnS. The percentage of photocatalytic dye removal in the presence of MNPs@BNPs@ZnO–ZnS with ZnO:ZnS molar ratio: 0.75:0.25 was obtained for methyl orange (85%) and for methylene blue (80.5%) under ultraviolet light (Fig. 10a and c). The amount of catalyst is 0.08 g and the time of each test is 90 min. The rate of photocatalytic dye removal of MO and MB aqueous solutions at maximal absorption (λ max) for each dye was investigated. The maximum absorption wavelength is 466 nm for methyl orange and 664 nm for methylene blue.

The reproducibility of dye removal reactions for methylene blue and methyl orange was investigated several times (four times) under optimal conditions. As expected, the dye degradation reactions of methyl orange and methylene blue showed excellent reproducibility, and the dye removal efficiencies for methyl orange and methylene blue were 85% and 80.5%, respectively, every four times.

After the calculations, the pseudo-first-order kinetics for dye degradation was obtained. Also, the rate constant is obtained from the following equation:

$$Ln(A_t / A_0) = ln(C_t / C_0) = -k_{app}t \quad (3)$$

In this equation, $C_0$ is the concentration of organic dye at initial and $C_t$ is the concentration of organic dye at time t.

Kinetic and $K_{ap}$ diagrams of photocatalytic dye removal of these dyes are shown in Fig. 10 b, d. The dye removal rate constant was obtained for MO (0.0181 $min^{-1}$) and for MB (0.0171 $min^{-1}$). Based on the obtained results, the photocatalytic dye removal process of MO and MB dyes follows the first-order velocity equation.

Then, the effect of increasing the concentration of aqueous solutions of dyes on the amount of dye removal in the presence of photocatalyst, under ultraviolet light was investigated. Dye removal results for different concentrations of MB and MO are summarized in Table 3.

The achieved kinetic parameters for photocatalytic dye removal of MO and MB dyes under visible and ultraviolet light are illustrated in Table 4.

### 3.3. The effect of pH on the dye removal process

The pH of the solution can be one of the factors affecting the photocatalytic removal process, so the removal of methyl orange and methylene blue at different pHs (3, 5, 8 and 11) under ultraviolet light was investigated. The results of photocatalytic dye removal with MNPs@ BNPs@ZnO–ZnS under ultraviolet light for MO and MB are shown in Fig. S6 (see the supporting file). In photocatalytic dye removal, in most cases, the dye molecule must first be absorbed on the photocatalyst surface, and then the light molecule is destroyed by light radiation. After examining the removal of methyl orange dye at different pHs, the rate of degradation of this dye in pH = 7 (80.5%) is higher than other pHs. The reason for this is related to the nature of the dye and surface charge of the photocatalyst. Methyl orange is an anionic azo dye and the surface charge of the photocatalyst is negative, so there is an electrostatic repulsion for the initial absorption of the dye on the surface of the photocatalyst. It should be noted that at pH 3, which has a lower amount of negative charge (−2.5 mV), the removal of MO is higher than at pH 5 and 8. Even though the negative charge on the surface is less, the electrostatic repulsion is less and as a result, the amount of dye degradation is higher. Methylene blue is a cationic dye and the surface charge of the photocatalyst is negative at pH 3, 5, and 8. At pH 8, there are more negative charges on the surface, the amount of dye absorption on the photocatalyst surface is higher due to electrostatic attraction, as a result, the percentage of dye degradation increases.

The dye removal at pH 7 for methylene blue is 80.5%. The degradation rate for MB is higher at alkaline pHs, which can be justified by the amount of negative charge on the photocatalyst surface at pHs 8 and 11. Based on the zeta potential, as we move towards higher

**Table 3**
The effect of increasing the concentration of MO and MB dyes on the dye removal efficiency.

| Entry | Catalyst* | Dye removal (%) | Dye | Concentration (ppm) | Light |
|---|---|---|---|---|---|
| **1** | MNPs@BNPs@ZnO–ZnS | 85 | MO | 10 | UV |
| **2** | MNPs@BNPs@ZnO–ZnS | 82.2 | MO | 15 | UV |
| **3** | MNPs@BNPs@ZnO–ZnS | 77.5 | MO | 20 | UV |
| **4** | MNPs@BNPs@ZnO–ZnS | 71.5 | MO | 50 | UV |
| **5** | MNPs@BNPs@ZnO–ZnS | 80.5 | MB | 10 | UV |
| **6** | MNPs@BNPs@ZnO–ZnS | 76.5 | MB | 15 | UV |
| **7** | MNPs@BNPs@ZnO–ZnS | 72.4 | MB | 20 | UV |
| **8** | MNPs@BNPs@ZnO–ZnS | 68 | MB | 50 | UV |

*: Optimal catalyst with molar ratio ZnO/ZnS: 0.75/0.25

**Table 4**
Kinetic parameters for the photocatalytic dye removal process.

| Light | Photocatalyst | $R^2$ | $K_{ap}$ ($min^{-1}$) | Dye |
|---|---|---|---|---|
| Uv | MNPs@BNPs@ZnO–ZnS | 0.9904 | 0.0186 | MO |
| Uv | MNPs@BNPs@ZnO–ZnS | 0.9883 | 0.0171 | MB |

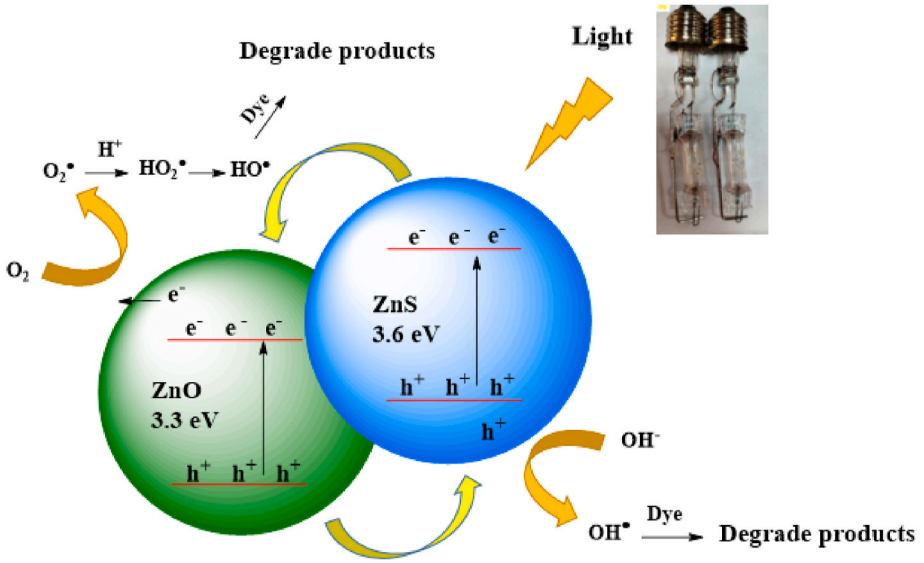


**Scheme 2.** Photocatalytic degradation of organic dyes in the presence of $Fe_3O_4$@BNPs@ZnO–ZnS.

pH (alkaline), the amount of negative charge on the surface of the photocatalyst increases, so the dye is absorbed quickly and destroyed easily.

### 3.4. Probable mechanism and active radical species

Photocatalytic degradation processes for MO and MB are illustrated equations (3)–(7) and Scheme 2. First, electrons and holes are created by irradiating light photon to ZnS. Electron transfer is from VB of zinc sulfide to VB of zinc oxide and hole transfer is from CB of zinc oxide to CB of zinc sulfide [66].

$$ZnS + h\upsilon \rightarrow h^+ + e \quad (4)$$

The oxidation and reduction reactions that occur on the surface of the photocatalyst are:

$$OH^- + h^+ \rightarrow {}^{\bullet}OH \quad (5)$$

$$H_2O + h^+ \rightarrow {}^{\bullet}OH + H^+ \quad (6)$$

$$O_2 + e^- \rightarrow O_2^{\bullet -} + H^+ \rightarrow HO_2^{\bullet} \quad (7)$$

Adsorbed water and hydroxyl anion are the source of hydroxyl radicals. In photocatalytic processes, active species such as $^{\bullet}OH$, $O_2^{\bullet -}$, $HO_2^{\bullet}$, $h^+$, $e^-$ are responsible for the degradation of dyes and organic pollutants [67,68]. The conversion of dangerous and toxic dyes in the presence of $^{\bullet}OH$ and $O_2^{\bullet -}$ radicals on the surface of MNPs@ BNPs@ZnO–ZnS into substances such as water and carbon dioxide are completely in line with the goals of green chemistry. The presence of oxygen in the photocatalytic process prohibits the recombination of electrons and holes.

$$\text{Dye (MO or MB)} + \bullet OH \text{ or } O_2^{\cdot -} \rightarrow CO_2 + H_2O \text{ and other products} \quad (8)$$

Reactive species such as $^{\bullet}OH$, $O_2^{\cdot -}$, $HO_2\cdot$, $h^+$, are responsible for the initiation of redox reactions and decompose MB dye into $CO_2$, $H_2O$ or mineral ions. Therefore, the color of MB and MO becomes colorless due to the destruction of aromatic rings [69–72] (Scheme 3).

In order to determine the role of active species and their effect in the photocatalytic process, compounds such as ascorbic acid, isopropyl alcohol, citric acid and sodium nitrate were used as scavengers for $O_2^{\cdot -}$, ·OH, holes ($h^+$) and aqueous electrons ($e^-$), respectively [73] (Fig. 11).

Based on the results, the order of activity of the species according to their effect in the photocatalytic degradation process of MB is as follows: $\cdot OH > O_2^{\cdot -} >$ hole > electron.

The efficiency of $Fe_3O_4$@BNPs@ZnO–ZnS was compared with some other photocatalytic systems (Table 5). As shown, this photocatalyst is superior to most photocatalysts in parameters such as time, efficiency and type of light source used. In this study, 125-W high-pressure mercury lamps were used as a low-cost and high-efficiency UV light source.

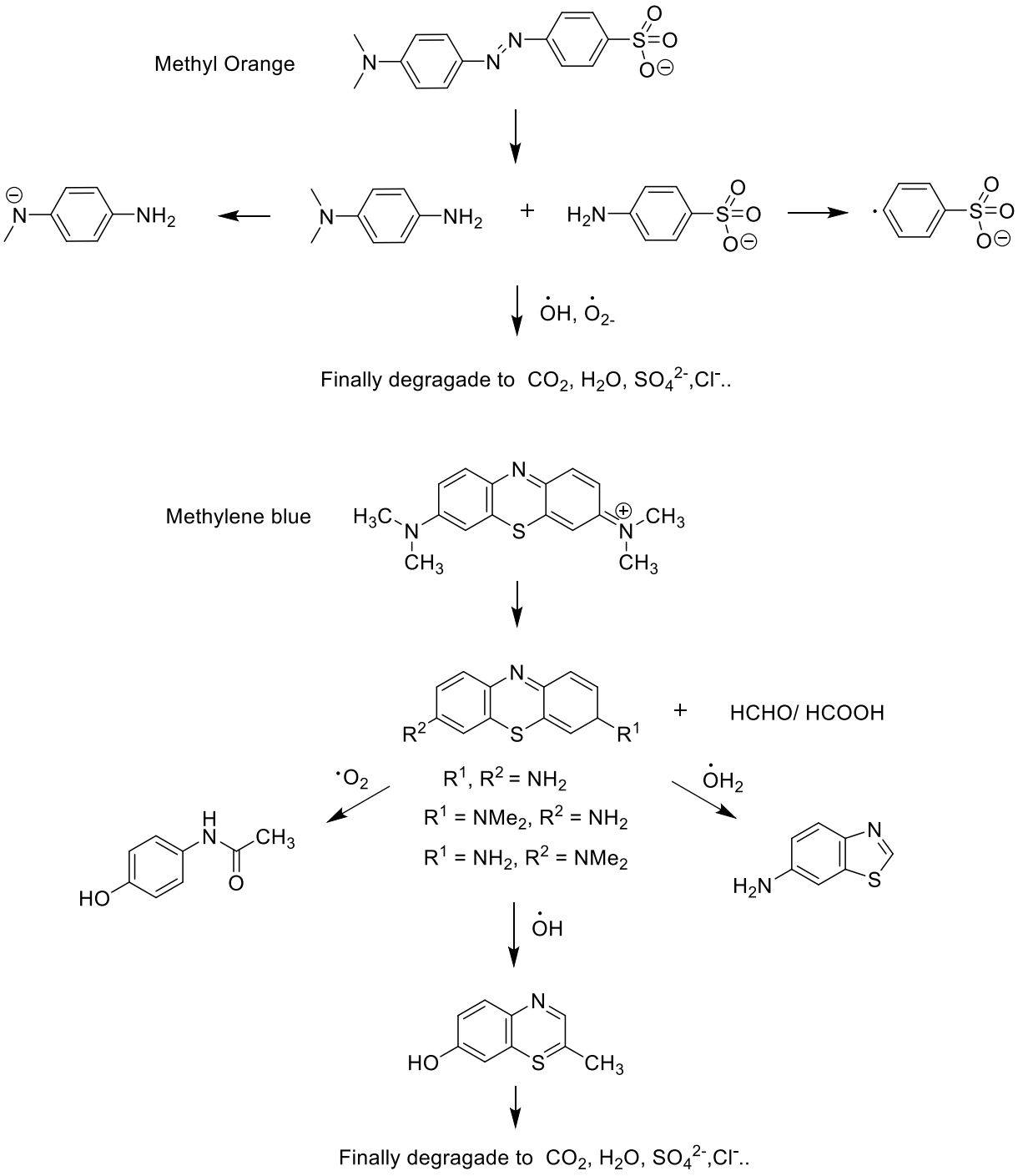


**Scheme 3.** Proposed compounds of MO and MB photocatalytic degradation.

### *3.5. Total organic carbon analysis*

In the process of water purification, one of the important factors is to determine the total amount of organic carbon. The amount of TOC has a great impact on the health, taste and smell of water, so in the processes of dye removal and water purification, efforts are made to reduce the amount of TOC [82]. The total organic carbon (TOC) measurement test for cationic and anionic dyes was performed before and after the photocatalytic reaction. The values of TOC are shown in Table 6. According to Tables 6 and in the photocatalytic dye removal process in the presence of $Fe_3O_4$@BNPs@ZnO–ZnS, the amount of TOC has decreased significantly, which

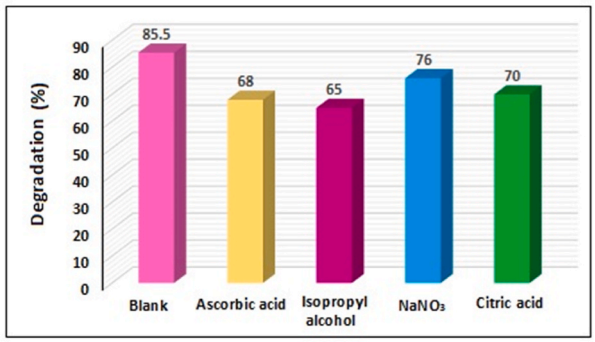


**Fig. 11.** Effect of radical scavengers on the photocatalytic degradation of MB in the presence of $Fe_3O_4$@BNPs@ZnO–ZnS.

**Table 5**
Comparison of photocatalytic performance of $Fe_3O_4$@BNPs@ZnO–ZnS with some other photocataysts.

| Catalyst | Light sources | Dye | Degradation (%), Time (min) | Ref. |
|---|---|---|---|---|
| ZnO + Alginate 2% | UV | MB | 63%, 240 | [74] |
| ZnO–ZnS–$MnO_2$ | Visible light | MB | 97%, 140 | [54] |
| Cs–ZnS-NPs | UV | Acid brown | 92%, 180 | [75] |
| ZnO@ZnS CSNPs | UV | Congo red | 85%, 120 | [76] |
| ZnO–ZnS nanowire | Hg-arc (300 W) | MO | 90%, 40 | [66] |
| ZnO@ZnS core–shell | UV | Rose Bengal | pH = 4, 51%, pH = 7, 50%, 120 | [77] |
| Chitosan-ZnS-NPs | UV | Acid Black 234 | 92.6% | [75] |
| ZnS–CdS | Uv–visible | MO | 44.1%. 120 | [78] |
| ZnO NPs | UV | MB | 55%, 90 | [79] |
| Ag–AgBr–ZnO | Sunlight | RhB | 90%, 60 min | [80] |
| Ag–ZnO | Sunlight | MB | 72%, 120 min | [81] |
| $Fe_3O_4$@BNPs@ZnO–ZnS | Mercury lamp 125 (UV) | MB, MO | 85% (MB), MO (80.5%), 90 | This work |

**Table 6**
Determination of TOC for cationic and anionic dyes.

| Dye | Dye concentration (ppm) | TOC (mg/L) before decomposition | TOC (mg/L) after decomposition |
|---|---|---|---|
| MO | 10 | 9.5 | 1.47 |
| MO | 15 | 14.35 | 2.52 |
| MO | 20 | 19.2 | 365 |
| MB | 10 | 9.3 | 1.82 |
| MB | 15 | 14.5 | 3.10 |
| MB | 20 | 19.60 | 4.10 |

indicates the efficiency of the prepared photocatalyst.

### *3.6. Reusability of the photocatalyst*

After examining parameters such as the amount of photocatalyst, the concentration of dye, the type of light source and the effect of pH on the photocatalytic removal process, the reusability of photocatalyst was also surveyed.

The reusability of MNPs@BNPs@ZnO–ZnS under ultraviolet light for aqueous solutions of MO and MB (10 ppm) up to 5 times was evaluated and the results are shown in Table 7. A slight decrease in photocatalyst efficiency was observed after five uses (4%), which could be due to the blockage of the active sites of the photocatalyst surface by the dye.

In order to understand the exact amount of ZnO and ZnS on the surface of the nanocomposite, ICP-OES analysis was performed. Based on the results, there are 6.45 mmol of zinc sulfide and 20.65 mmol of zinc oxide on the surface per gram of the photocatalyst. After calculations, the amount of ZnS was 23.75%, and the amount of ZnO was 76.25%.

### *3.7. Decolorization of industrial wastewaters*

In order to evaluate the efficiency of the photocatalyst, dye removal from textile, carton and spinning effluents in the presence of UV light and in the absence of catalyst for 30–90 min was investigated. After the elapsed time, the amount of photolysis was 3%, 3% and 4%, respectively. Also, in order to find out how much of the dye is absorbed by the photocatalyst surface, the dye removal of the textile, carton and spinning wastewaters in the presence of the photocatalyst and in the absence of UV light were evaluated at ambient

**Table 7**
Ability to retrieve MNPs@BNPs@ZnO–ZnS to remove MO and MB colors under ultraviolet light.

| Run | MO | MB |
|---|---|---|
| 1 | 85 | 80.5 |
| 2 | 85 | 80.5 |
| 3 | 84 | 79 |
| 4 | 83 | 78 |
| 5 | 81 | 76 |

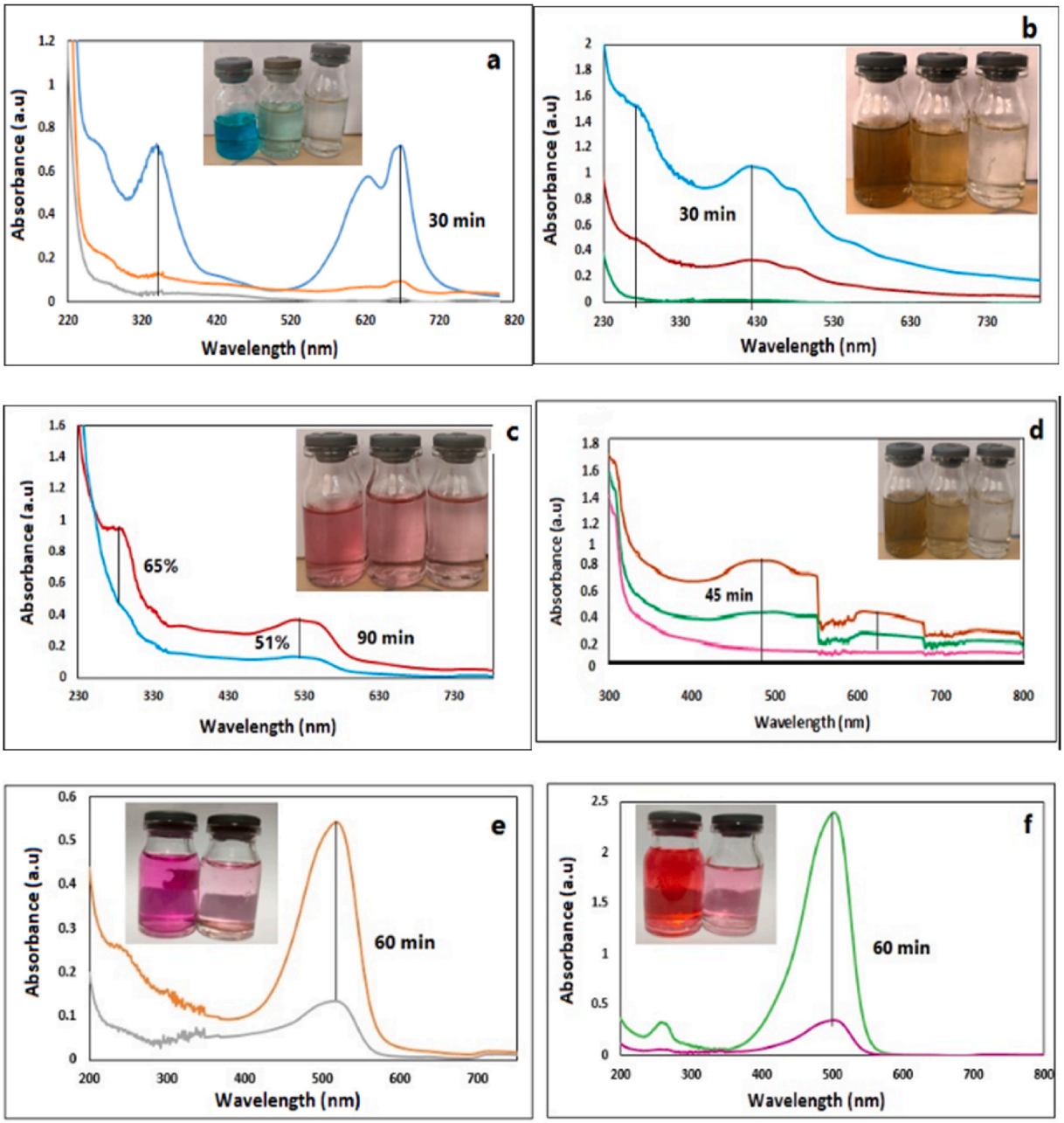


**Fig. 12.** Optical absorbance spectra for (a) benton (15 ppm), (b) dark olive (20 ppm), (c) pastel pink (15 ppm), (d) carton wastewater (25 ppm), (e) magenta dye of spinning mill and (f) red color of the spinning mill (25 ppm). (For interpretation of the references to color in this figure legend, the reader is referred to the Web version of this article.)

temperature in 90 min. After that, wastewater solutions were examined by UV–visible spectrophotometer and the percentage of adsorbed dye on the photocatalyst surface was 2%, 3% and 3%, respectively. Based on the results, it can be understood that the decolorization process in the presence of the photocatalyst is based on the degradation process, not the adsorption. It should be noted that photocatalytic decolorization requires the presence of both photocatalyst and UV light source.

The dye removal time for the actual effluent varied between 30 and 90 min, depending on the type of the dye. Also, the higher the effluent concentration, the less the dye removal in 90 min. Carton effluents with concentrations of 100, 50, 25 and 10 ppm were examined which showed 87%, 93.2%, 98.1% and 99.7% decolorization in the presence of MNPs@BNPs@ZnO–ZnS and at ambient temperature, respectively.

Three textile effluents (pastel pink, benton, dark olive colors, with initial concentrations of 15–25 ppm) were evaluated in the presence of MNPs@BNPs@ZnO–ZnS under UV light at ambient temperature. It is worth noting that in all experiments the reactor was placed in a container of cold water to keep the temperature constant.

Benton and dark olive dye effluents were almost completely decolorized with 98.3% and 99.7% efficiency in 20–30 min. But sausage-colored effluent in about 90 min showed about 65% dye removal (Fig. 12 a-c). Carton effluent with a concentration of 20 ppm was also examined and its dye removal diagram is shown in Fig. 12d.

Also, the effluents of the spinning mill (magenta and red) were evaluated with high-pressure mercury lamps without bubbles in the presence of 0.08 g of photocatalyst (Fig. 12e-f). The decolorization rate was 76% for magenta effluent and 85.7 for red effluent after 60 min.

It seems that effluents containing cationic dyes become completely colorless in the presence of MNPs@BNPs@ZnO–ZnS (0.08 g) because the photocatalyst surface has a negative charge in most pHs. The mentioned photocatalyst has excellent capability in removing dye from industrial effluents in relatively short times with remarkable efficiency.

It is worth noting that MNPs@BNPs@ZnO–ZnS is also active in the visible area. Therefore, all industrial effluents were studied under visible light. The carton, textile and spinning effluents were examined in the presence of visible lamp (high-pressure mercury lamp) in 60–90 min. Carton, benton, dark olive, sausage, magenta and red effluents showed 60% (90 min), 62% (60 min), 58% (60 min), 30% (90 min), 38% (90 min) and 48% (60 min) of dye removal under optimal conditions, respectively.

## 4. Conclusions

Due to the increase of emerging pollutants in water, the use of modern treatment technology, including the use of advanced oxidation methods (AOPs), biological methods, biodegradability, and photocatalytic reactions to compensate for the defects of traditional wastewater treatment methods, has received much attention [83–86]. Biological treatment and photocatalytic reactions have shown great potential as a low-cost, environmentally friendly and sustainable treatment technology [87,88].

Therefore, in the near future, the use of environmentally compatible heterogeneous photocatalysts are very suitable candidates for replacing the old inappropriate, expensive and environmentally incompatible methods.

Here, we introduced MNPs@BNPs@ZnO–ZnS (with molar ratio of ZnO:ZnS = 0.75:0.25) as a novel, reusable photocatalyt for decolorization of MB, MO and real wastewaters. The designed magnetic nanocomposite can remove MB (80.5%), MO (85%) and real wastewater with 60–99% efficiency in a short time (30–90 min) in the presence of high-pressure mercury lamp.

Photocatalyst is synthesized in a simple process and in easy conditions without the need for special temperatures and pressures. The synthesized photocatalyst is active in both the UV and visible light regions, but showed the best performance in the UV region. According to the TGA diagram, the MNPs@BNPs@ZnO–ZnS is stable and lost only 6.124% of its weight. One of the interesting results obtained in this method is the reproducibility of dye removal results in the presence of MNPs@BNPs@ZnO–ZnS. The light sources used are high-pressure mercury lamps that are very cheap, durable and efficient which are very economical and efficient compared to UV lamps on the market. It is worth mentioning that the introduced photocatalyst can be used to remove dye in textile, dyeing and similar industries.

## Additional information

Supplementary content related to this article has been published online at [URL].

## Author contribution statement

Minoo Khodamorady: Conceived and designed the experiments; Performed the experiments; Analyzed and interpreted the data; Wrote the paper. Kiumars Bahrami: Conceived and designed the experiments; Analyzed and interpreted the data; Contributed reagents, materials, analysis tools or data; Wrote the paper.

## Data availability statement

Data will be made available on request.

## Declaration of competing interest

There is no declaration of interests.

## Acknowledgments

The authors are extremely grateful of the Razi University Research Council for support. Also, this study is a project with the number 99026741 under the financial support of the Iran National Science Foundation (INSF).

## Appendix A. Supplementary data

Supplementary data related to this article can be found at https://doi.org/10.1016/j.heliyon.2023.e16397.

## References

[1] M. Khosravi, A.S. Maddah, N. Mehrdadi, G.N. Bidhendi, M. Baghdadi, Synthesis of $TiO_2$/ZnO electrospun nanofibers coated-sewage sludge carbon for adsorption of Ni (II), Cu (II), and COD from aqueous solutions and industrial wastewaters, J. Dispersion Sci. Technol. 42 (2021) 802–812.
[2] V.C. Santos-Ebinuma, I.C. Roberto, M.F. Simas Teixeira, A. Pessoa Jr., Improving of red colorants production by a new Penicillium purpurogenum strain in submerged culture and the effect of different parameters in their stability, Biotechnol. Prog. 29 (2013) 778–785.
[3] M.A. Ashraf, M.M. Hanafiah, Sustaining Life on Earth System through Clean Air, Pure Water, and Fertile Soil, Springer, 2019, pp. 13679–13680.
[4] A.K. Sahoo, S.K. Srivastava, P.K. Raul, A.K. Gupta, R. Shrivastava, Graphene nanocomposites of CdS and ZnS in effective water purification, J. Nanoparticle Res. 16 (2014) 1–17.
[5] Y.J. Dhir, Hazards of fashion and textile waste: approaches for effective waste management, in: Waste Management in the Fashion and Textile Industries, Elsevier, 2021, pp. 31–58.
[6] J. Paul, K. Rawat, K. Sarma, S. Sabharwal, Decoloration and degradation of Reactive Red-120 dye by electron beam irradiation in aqueous solution, Appl. Radiat. Isot. 69 (2011) 982–987.
[7] M. Wang, N. Chamberland, L. Breau, J.-E. Moser, R. Humphry-Baker, B. Marsan, S.M. Zakeeruddin, M. Grätzel, An organic redox electrolyte to rival triiodide/iodide in dye-sensitized solar cells, Nat. Chem. 2 (2010) 385–389. https://www.nature.com/articles/nchem.610.
[8] M.W. Alam, M. Aamir, M. Farhan, M. Albuhulayqah, M.M. Ahmad, C. Ravikumar, V. Dileep Kumar, H. Ananda Murthy, Green synthesis of Ni-Cu-Zn based nanosized metal oxides for photocatalytic and sensor applications, Crystals 11 (2021) 1467.
[9] Z.A. Messaoudi, D. Lahcene, T. Benaissa, M. Messaoudi, B. Zahraoui, M. Belhachemi, A. Choukchou-Braham, Adsorption and photocatalytic degradation of crystal violet dye under sunlight irradiation using natural and modified clays by zinc oxide, Chem. Methodol. 6 (2022) 661–676.
[10] I. Amar, A. Sharif, M. Ali, S. Alshareef, F. Altohami, M. Abdulqadir, M. Ahwidi, Removal of methylene blue from aqueous solutions using nano-magnetic adsorbent based on zinc-doped cobalt ferrite, Chem. Methodol. 4 (2020) 1–18.
[11] S. Taghavi Fardood, F. Moradnia, S. Moradi, R. Forootan, F. Yekke Zare, M. Heidari, Eco-friendly synthesis and characterization of α-$Fe_2O_3$ nanoparticles and study of their photocatalytic activity for degradation of Congo red dye, Nano Res. 4 (2019) 140–147.
[12] S. Taghavi Fardood, F. Moradnia, A.H. Ghalaichi, S. Danesh Pajouh, M. Heidari, Facile green synthesis and characterization of zinc oxide nanoparticles using tragacanth gel: investigation of their photocatalytic performance for dye degradation under visible light irradiation, Nano Res. 5 (2020) 69–76.
[13] A. Phuruangrat, A. Maneechote, P. Dumrongrojthanath, N. Ekthammathat, S. Thongtem, T. Thongtem, Effect of pH on visible-light-driven $Bi_2WO_6$ nanostructured catalyst synthesized by hydrothermal method, Superlattice. Microst. 78 (2015) 106–115.
[14] R. Fatima, M.F. Warsi, M.I. Sarwar, I. Shakir, P.O. Agboola, M.F.A. Aboud, S. Zulfiqar, Synthesis and characterization of hetero-metallic oxides-reduced graphene oxide nanocomposites for photocatalytic applications, Ceram. Int. 47 (2021) 7642–7652.
[15] L. Yang, Z. Zhao, H. Wang, J. Dong, L. Wang, Q. Zhou, X. Wan, R. Zhao, Z. Cai, Synthesis of ZnO/ZnS core/shell microsphere and its photocatalytic activity for methylene blue and eosin dyes degradation, J. Dispersion Sci. Technol. 41 (2020) 2152–2158.
[16] Y. Li, L.-X. Shan, X.-X. Lian, Q.-J. Zhou, D.-M. An, Enhanced $NO_2$ sensing performance of ZnO@ ZnS core-shell structure fabricated using a solution chemical method, Ceram. Int. 47 (2021) 27411–27419.
[17] B. Hadzic, B. Matovic, M. Randjelovic, R. Kostic, M. Romcevic, J. Trajic, N. Paunovic, N. Romcevic, Phonons investigation of ZnO@ ZnS core-shell nanostructures with active layer, J. Raman Spectrosc. 52 (2021) 616–625.
[18] W. Li, G. Song, F. Xie, M. Chen, Y. Zhao, Preparation of spherical ZnO/ZnS core/shell particles and the photocatalytic activity for methyl orange, Mater. Lett. 96 (2013) 221–223.
[19] S. Goktas, A. Goktas, A comparative study on recent progress in efficient ZnO based nanocomposite and heterojunction photocatalysts: a review, J. Alloys Compd. 863 (2021), 158734.
[20] Q. Zhang, J. Li, M. Xu, Ag decorated ZnO based nanocomposites for visible light-driven photocatalytic degradation: basic understanding and outlook, J. Phys. D Appl. Phys. 55 (2022) 483001.
[21] M. Abdul Hassan, S. Hassan, K. Hassan, Green and chemical synthesis of bimetallic nanoparticles (Fe/Ni) supported by zeolite 5A as a heterogeneous fenton-like catalyst and study of kinetic and thermodynamic reaction for decolorization of reactive red 120 dye from aqueous pollution, Eurasian Chem. Commun. 4 (2022) 1062–1086.
[22] I. Karm, A. Dwaish, O. Dakhil, Algae extracts as reduction agents for biosynthesis of silver nanoparticles for alternative medicinal compounds, Eurasian Chem Commun 4 (2022) 910–920.
[23] S. Sarli, N. Ghasemi, Optimization of biosynthesized Zn nanoparticles by poisonous Taxus baccata leaves extract and evaluation of their effect on the bacterias and MCF-7 cancer cells, Eurasian Chem. Commun 2 (2020) 302–318.
[24] F. Moradnia, A. Ramazani, S.T. Fardood, F. Gouranlou, A novel green synthesis and characterization of tetragonal-spinel $MgMn_2O_4$ nanoparticles by tragacanth gel and studies of its photocatalytic activity for degradation of reactive blue 21 dye under visible light, Mater. Res. Express 6 (2019), 075057.
[25] Z. Xin, L. Li, W. Zhang, T. Sui, Y. Li, X. Zhang, Synthesis of ZnS@ CdS–Te composites with p–n heterostructures for enhanced photocatalytic hydrogen production by microwave-assisted hydrothermal method, Mol. Catal. 447 (2018) 1–12.
[26] F. Moradnia, S.T. Fardood, A. Ramazani, B.-k. Min, S.W. Joo, R.S. Varma, Magnetic $Mg_{0.5}Zn_{0.5}FeMnO_4$ nanoparticles: green sol-gel synthesis, characterization, and photocatalytic applications, J. Clean. Prod. 288 (2021), 125632.
[27] S.H. Gebre, M.G. Sendeku, New frontiers in the biosynthesis of metal oxide nanoparticles and their environmental applications: an overview, SN Appl. Sci. 1 (2019) 1–28.
[28] B. Kumar, K. Smita, L. Cumbal, A. Debut, Y. Angulo, Biofabrication of copper oxide nanoparticles using Andean blackberry (Rubus glaucus Benth.) fruit and leaf, J. Saudi Chem. Soc. 21 (2017) S475–S480.
[29] L. Liu, Y. Chen, T. Guo, Y. Zhu, Y. Su, C. Jia, M. Wei, Y. Cheng, Chemical conversion synthesis of ZnS shell on ZnO nanowire arrays: morphology evolution and its effect on dye-sensitized solar cell, ACS Appl. Mater. Interfaces 4 (2012) 17–23.
[30] I. Elmehasseb, S. Kandil, K. Elgendy, Advanced visible-light applications utilizing modified Zn-doped $TiO_2$ nanoparticles via non-metal in situ dual doping for wastewater detoxification, Optik 213 (2020), 164654.
[31] Q. Zhou, L. Li, Z. Xin, Y. Yu, L. Wang, W. Zhang, Visible light response and heterostructure of composite CdS@ ZnS–ZnO to enhance its photocatalytic activity, J. Alloys Compd. 813 (2020), 152190.

[32] M. Nemiwal, T.C. Zhang, D. Kumar, Recent progress in g-$C_3N_4$, $TiO_2$ and ZnO based photocatalysts for dye degradation: strategies to improve photocatalytic activity, Sci. Total Environ. 767 (2021), 144896.
[33] X. Zheng, F. Kang, C. Huang, S. Lv, J. Zhang, H. Peng, Enhanced photocatalytic capacity of ZnS–ZnO–$Sm_2O_3$ composites for the removal of dyes and antibiotics in visible light region, J. Ind. Eng. Chem. 88 (2020) 186–195.
[34] O. Yayapao, T. Thongtem, A. Phuruangrat, S. Thongtem, Sonochemical synthesis of Dy-doped ZnO nanostructures and their photocatalytic properties, J. Alloys Compd. 576 (2013) 72–79.
[35] J. Akhtar, M. Tahir, M. Sagir, H.S. Bamufleh, Improved photocatalytic performance of Gd and Nd co-doped ZnO nanorods for the degradation of methylene blue, Ceram. Int. 46 (2020) 11955–11961.
[36] O. Yayapao, T. Thongtem, A. Phuruangrat, S. Thongtem, Ultrasonic-assisted synthesis of Nd-doped ZnO for photocatalysis, Mater. Lett. 90 (2013) 83–86.
[37] P. Dumrongrojthanath, T. Thongtem, A. Phuruangrat, S. Thongtem, Synthesis and characterization of hierarchical multilayered flower-like assemblies of Ag doped $Bi_2WO_6$ and their photocatalytic activities, Superlattice. Microst. 64 (2013) 196–203.
[38] N.C. Birben, C.S. Uyguner-Demirel, S.S. Kavurmaci, Y.Y. Gürkan, N. Turkten, Z. Cinar, M. Bekbolet, Application of Fe-doped $TiO_2$ specimens for the solar photocatalytic degradation of humic acid, Catal. Today 281 (2017) 78–84.
[39] J. Zhang, S. Liu, J. Yu, M. Jaroniec, A simple cation exchange approach to Bi-doped ZnS hollow spheres with enhanced UV and visible-light photocatalytic $H_2$-production activity, J. Mater. Chem. 21 (2011) 14655–14662.
[40] K.K. Kefeni, T.A. Msagati, B.B. Mamba, Ferrite nanoparticles: synthesis, characterisation and applications in electronic device, J. Mater. Sci. Eng. B. 215 (2017) 37–55.
[41] Y.L. Pang, S. Lim, H.C. Ong, W.T. Chong, Research progress on iron oxide-based magnetic materials: synthesis techniques and photocatalytic applications, Ceram. Int. 42 (2016) 9–34.
[42] M. Shekofteh-Gohari, A. Habibi-Yangjeh, M. Abitorabi, A. Rouhi, Magnetically separable nanocomposites based on ZnO and their applications in photocatalytic processes: a review, Crit. Rev. Environ. Sci. Technol. 48 (2018) 806–857.
[43] M. Khodamorady, K. Bahrami, $Fe_3O_4$@ BNPs-CPTMS-Chitosan-Pd (0) as an efficient and stable heterogeneous magnetic nanocatalyst for the chemoselective oxidation of alcohols and homoselective synthesis of 5-subestituted 1H-tetrazoles, ChemistrySelect 4 (2019) 8183–8194.
[44] M. Mohammadi, M. Khodamorady, B. Tahmasbi, K. Bahrami, A. Ghorbani-Choghamarani, Boehmite nanoparticles as versatile support for organic-inorganic hybrid materials: synthesis, functionalization, and applications in eco-friendly catalysis, J. Ind. Eng. Chem. 97 (2021) 1–78.
[45] Y. Liu, L. Yu, Y. Hu, C. Guo, F. Zhang, X.W.D. Lou, A magnetically separable photocatalyst based on nest-like γ-$Fe_2O_3$/ZnO double-shelled hollow structures with enhanced photocatalytic activity, Nanoscale 4 (2012) 183–187.
[46] J. Xie, Z. Zhou, Y. Lian, Y. Hao, P. Li, Y. Wei, Synthesis of α-$Fe_2O_3$/ZnO composites for photocatalytic degradation of pentachlorophenol under UV–vis light irradiation, Ceram. Int. 41 (2015) 2622–2625.
[47] M.F. Sanad, A.E. Shalan, S.M. Bazid, S.M. Abdelbasir, Pollutant degradation of different organic dyes using the photocatalytic activity of ZnO@ ZnS nanocomposite materials, J. Environ. Chem. Eng. 6 (2018) 3981–3990.
[48] G. Hitkari, S. Singh, G. Pandey, Photoluminescence behavior and visible light photocatalytic activity of ZnO, ZnO/ZnS and ZnO/ZnS/α-$Fe_2O_3$ nanocomposites, Trans. Nonferrous Metals Soc. China 28 (2018) 1386–1396.
[49] T. Xu, P. Wang, D. Wang, K. Zhao, M. Wei, X. Liu, H. Liu, J. Cao, Y. Chen, H. Fan, Ultrasound-assisted synthesis of hyper-dispersed type-II tubular $Fe_3O_4$@$SiO_2$@ ZnO/ZnS core/shell heterostructure for improved visible-light photocatalysis, J. Alloys Compd. 838 (2020), 155689.
[50] P. Wei, X. Yu, Y. Li, Preparation of $Fe_3O_4$/ZnO/ZnS Composites with enhanced photoperformance under solar irradiation, J. Electron. Mater. 48 (2019) 4877–4885.
[51] P.V. Raleaooa, A. Roodt, G.G. Mhlongo, D.E. Motaung, R.E. Kroon, O.M. Ntwaeaborwa, Luminescent, magnetic and optical properties of ZnO-ZnS nanocomposites, Phys. B 507 (2017) 13–20.
[52] K. Liu, Y. Qin, Y. Muhammad, Y. Zhu, R. Tang, N. Chen, H. Shi, H. Zhang, Z. Tong, B. Yu, Effect of $Fe_3O_4$ content and microwave reaction time on the properties of $Fe_3O_4$/ZnO magnetic nanoparticles, J. Alloys Compd. 781 (2019) 790–799.
[53] S. Khan, J.S. Han, S.Y. Lee, S.H. Cho, ZnS Nano-spheres formed by the aggregation of small crystallites and their photocatalytic degradation of eosin B, Chin. J. Chem. 35 (2017) 159–164.
[54] M. Abdullah, P. John, Z. Ahmad, M.N. Ashiq, S. Manzoor, M.I. Ghori, M.U. Nisa, A.G. Abid, K.Y. Butt, S. Ahmed, Visible-light-driven ZnO/ZnS/$MnO_2$ ternary nanocomposite catalyst: synthesis, characterization and photocatalytic degradation of methylene blue, Appl. Nanosci. 11 (2021) 2361–2370.
[55] S. Jindal, S.M. Giripunje, S.B. Kondawar, Electronic and optical properties of size-controlled ZnO nanoparticles synthesized by a facile chemical approach, Iran. J. Chem. Chem. Eng. 38 (2019) 11–20.
[56] A. Beristain-Bautista, D. Olguín, S. Jiménez-Sandoval, n-to p-type conductivity transition and band-gap renormalization in ZnO:($Cu^+$Te) codoped films, Phys. Rev. Mater. 5 (2021), 065402.
[57] I.-D. Simandan, F. Sava, A.-T. Buruiana, I. Burducea, N. Becherescu, C. Mihai, A. Velea, A.-C. Galca, The effect of the deposition method on the structural and optical properties of ZnS thin films, Coatings 11 (2021) 1064.
[58] Y. Chen, X. Ren, K. Zhang, L. Wang, Structure and photoluminescence of ZnS/$CdS_{1-x}Se_x$ nanocomposite prepared by a two-step process, Mater. Sci. Semicond. Process. 100 (2019) 42–47.
[59] M. Sundararajan, P. Sakthivel, A.C. Fernandez, Structural, optical and electrical properties of ZnO-ZnS nanocomposites prepared by simple hydrothermal method, J. Alloys Compd. 768 (2018) 553–562.
[60] M. Khodamorady, S. Sohrabnezhad, K. Bahrami, Efficient one-pot synthetic methods for the preparation of 3,4-dihydropyrimidinones and 1, 4-dihydropyridine derivatives using BNPs@$SiO_2$ $(CH_2)_3NHSO_3H$ as a ligand and metal free acidic heterogeneous nano-catalyst, Polyhedron 178 (2020), 114340.
[61] Q. Feng, S. Li, W. Ma, H.-J. Fan, X. Wan, Y. Lei, Z. Chen, J. Yang, B. Qin, Synthesis and characterization of $Fe_3O_4$/ZnO-GO nanocomposites with improved photocatalytic degradation methyl orange under visible light irradiation, J. Alloys Compd. 737 (2018) 197–206.
[62] G. Li, R. Li, W. Zhou, A wire-shaped supercapacitor in micrometer size based on $Fe_3O_4$ nanosheet arrays on Fe wire, Nano-Micro Lett. 9 (2017) 1–8.
[63] K.S. Ranjith, R.B. Castillo, M. Sillanpaa, R.T.R. Kumar, Effective shell wall thickness of vertically aligned ZnO-ZnS core-shell nanorod arrays on visible photocatalytic and photo sensing properties, Appl. Catal. 237 (2018) 128–139.
[64] K. Bahrami, M. Khodamorady, Design of BNPs-TAPC palladium complex as a reusable heterogeneous nanocatalyst for the O-arylation of phenols and N-arylation of amines, Catal. Lett. 149 (2019) 688–698.
[65] S.S.G. Kumar, K.K. Rao, Comparison of modification strategies towards enhanced charge carrier separation and photocatalytic degradation activity of metal oxide semiconductors ($TiO_2$, $WO_3$ and ZnO), Appl. Surf. Sci. 391 (2017) 124–148.
[66] X. Gao, J. Wang, J. Yu, H. Xu, Novel ZnO–ZnS nanowire arrays with heterostructures and enhanced photocatalytic properties, CrystEngComm 17 (2015) 6328–6337.
[67] M.E. Khan, M.M. Khan, M.H. Cho, CdS-graphene nanocomposite for efficient visible-light-driven photocatalytic and photoelectrochemical applications, J. Colloid Interface Sci. 482 (2016) 221–232.
[68] N. Soltani, E. Saion, W.M.M. Yunus, M. Erfani, M. Navasery, G. Bahmanrokh, K. Rezaee, Enhancement of visible light photocatalytic activity of ZnS and CdS nanoparticles based on organic and inorganic coating, Appl. Surf. Sci. 290 (2014) 440–447.
[69] I.I. Khan, K. Saeed, I. Zekker, B. Zhang, A.H. Hendi, A. Ahmad, S. Ahmad, N. Zada, H. Ahmad, L.A. Shah, Review on methylene blue: its properties, uses, toxicity and photodegradation, Water 14 (2022) 242.
[70] W. Zhong, T. Jiang, Y. Dang, J. He, S.-Y. Chen, C.-H. Kuo, D. Kriz, Y. Meng, A.G. Meguerdichian, S.L. Suib, Mechanism studies on methyl orange dye degradation by perovskite-type $LaNiO_3$-δ under dark ambient conditions, Appl. Catal., A 549 (2018) 302–309.
[71] S.K. Kuila, R. Sarkar, P. Kumbhakar, P. Kumbhakar, C.S. Tiwary, T.K. Kundu, Photocatalytic dye degradation under sunlight irradiation using cerium ion adsorbed two-dimensional graphitic carbon nitride, J. Environ. Chem. Eng. 8 (2020), 103942.

[72] C. Yang, X. Wang, Y. Ji, T. Ma, F. Zhang, Y. Wang, M. Ci, D. Chen, A. Jiang, W. Wang, Photocatalytic degradation of methylene blue with ZnO@C nanocomposites: kinetics, mechanism, and the inhibition effect on monoamine oxidase A and B, NanoImpact 15 (2019), 100174.
[73] A. Krosuri, S. Wu, M.A. Bashir, M. Walquist, Efficient degradation and mineralization of methylene blue via continuous-flow electrohydraulic plasma discharge, J. Water Process Eng. 40 (2021), 101926.
[74] T. Tamer, W. Abou-Taleb, G. Roston, M. Mohyeldin, A. Omer, R. Khalifa, A. Hafez, Formation of zinc oxide nanoparticles using alginate as a template for purification of wastewater, Environ. Nanotechnol. Monit. Manag. 10 (2018) 112–121.
[75] A. Aziz, N. Ali, A. Khan, M. Bilal, S. Malik, N. Ali, H. Khan, Chitosan-zinc sulfide nanoparticles, characterization and their photocatalytic degradation efficiency for azo dyes, Int. J. Biol. Macromol. 153 (2020) 502–512.
[76] A. Sadollahkhani, O. Nur, M. Willander, I. Kazeminezhad, V. Khranovskyy, M.O. Eriksson, R. Yakimova, P.-O. Holtz, A detailed optical investigation of ZnO@ZnS core–shell nanoparticles and their photocatalytic activity at different pH values, Ceram. Int. 41 (2015) 7174–7184.
[77] A. Sadollahkhani, I. Kazeminezhad, J. Lu, O. Nur, L. Hultman, M. Willander, Synthesis, structural characterization and photocatalytic application of ZnO@ZnS core–shell nanoparticles, RSC Adv. 4 (2014) 36940–36950.
[78] H.-J. Wang, Y. Cao, L.-L. Wu, S.-S. Wu, A. Raza, N. Liu, J.-Y. Wang, T. Miyazawa, ZnS-based dual nano-semiconductors (ZnS/PbS, ZnS/CdS or ZnS/$Ag_2S$,): a green synthesis route and photocatalytic comparison for removing organic dyes, J. Environ. Chem. Eng. 6 (2018) 6771–6779.
[79] G. Hitkari, S. Singh, G. Pandey, Structural, optical and photocatalytic study of ZnO and ZnO–ZnS synthesized by chemical method, Nano-Struct. Nano-Objects 12 (2017) 1–9.
[80] Q. Zhang, C. Tian, A. Wu, Y. Hong, M. Li, H. Fu, In situ oxidation of Ag/ZnO by bromine water to prepare ternary Ag–AgBr/ZnO sunlight-derived photocatalyst, J. Alloys Compd. 563 (2013) 269–273.
[81] X. Chang, Z. Li, X. Zhai, S. Sun, D. Gu, L. Dong, Y. Yin, Y. Zhu, Efficient synthesis of sunlight-driven ZnO-based heterogeneous photocatalysts, Mater. Des. 98 (2016) 324–332.
[82] M. Khodamorady, M. Jafarzadeh, K. Bahrami, Design and introduction of BNPs@$SiO_2(CH_2)_3$-TAPC-O-$(CH_2)_2NH_2$-Pd (0) as an efficient nano-catalyst for the coupling reactions and removing of organic dyes, Inorg. Chem. Commun. 148 (2023), 110290.
[83] A. Sukhdev, M. Challa, L. Narayani, A.S. Manjunatha, P. Deepthi, J.V. Angadi, P.M. Kumar, M. Pasha, Synthesis, phase transformation, and morphology of hausmannite $Mn_3O_4$ nanoparticles: photocatalytic and antibacterial investigations, Heliyon 6 (2020), e03245.
[84] B.B. Garcia, G. Lourinho, P. Romano, P. Brito, Photocatalytic degradation of swine wastewater on aqueous $TiO_2$ suspensions: optimization and modeling via Box-Behnken design, Heliyon 6 (2020), e03293.
[85] A.M. Nasir, J. Jaafar, F. Aziz, N. Yusof, W.N.W. Salleh, A.F. Ismail, M. Aziz, A review on floating nanocomposite photocatalyst: fabrication and applications for wastewater treatment, J. Water Process Eng. 36 (2020), 101300.
[86] A. Haruna, I. Abdulkadir, S. Idris, Photocatalytic activity and doping effects of $BiFeO_3$ nanoparticles in model organic dyes, Heliyon 6 (2020), e03237.
[87] A. Pandey, R.R. Kumar, B. Kalidasan, I.A. Laghari, M. Samykano, R. Kothari, A.M. Abusorrah, K. Sharma, V. Tyagi, Utilization of solar energy for wastewater treatment: challenges and progressive research trends, J. Environ. Manag. 297 (2021), 113300.
[88] M. Yu, J. Wang, L. Tang, C. Feng, H. Liu, H. Zhang, B. Peng, Z. Chen, Q. Xie, Intimate coupling of photocatalysis and biodegradation for wastewater treatment: mechanisms, recent advances and environmental applications, Water Res. 175 (2020), 115673.